15

Understanding Mercury's Exosphere: Models Derived from MESSENGER Observations

ROSEMARY M. KILLEN, MATTHEW H. BURGER, RONALD J. VERVACK, JR., AND TIMOTHY A. CASSIDY

15.1 INTRODUCTION

Mercury's exosphere is quite complex, and a number of models have been developed to explain the observations presented in Chapter 14. The first models were based upon a few simple assumptions and primarily explored the dynamics of sodium atoms pushed anti-sunward by radiation pressure (e.g., Ip, 1986; Smyth and Marconi, 1995a, b). More recently, these early models have been superseded by simulations with an increasing number of interdependent processes (e.g., Leblanc and Johnson, 2003; Mura et al., 2009; Leblanc and Johnson, 2010; Burger et al., 2010, 2012, 2014). In this chapter, we briefly summarize the various source and loss processes before describing the published exosphere models, first for the three species observed almost continuously during the MESSENGER mission (Na, Mg, and Ca) by the Ultraviolet and Visible Spectrometer (UVVS) channel of the Mercury Atmospheric and Surface Composition Spectrometer (MASCS), and then more briefly for other species that have been observed or for which new upper limits have been derived.

Although a number of processes have been known for many years to be likely source and loss progenitors for surface-bounded exospheres, the complexity of the processes and the nature of line-of-sight observations require sophisticated and rigorous modeling of these various processes to discern their relative importance for each of the observed species populating the exosphere. In the next section we discuss five source processes: thermal desorption, impact vaporization, photon-stimulated desorption, ion sputtering, and chemical sputtering. Thermal desorption is a function of surface temperature, which varies not only with solar zenith angle but also with heliocentric distance. In addition, thermal desorption is a function of the binding energy of the atom with the surface, which can be a complicated function of the space weathering history of the surface grains and the fractional coverage of the adsorbate. Impact vaporization is a process that produces ejecta at a high temperature, which decreases with decreasing impact angle relative to the horizontal (Schultz, 1996). This temperature can be several thousand kelvin for silicates, but the precise temperature is not well determined. The vapor released as a function of impactor mass is a steep function of impact velocity and also depends on the relative densities of impactor and target and their compositions. Meteoroid and cometary impact is the most important process in regolith gardening, the pulverization and overturn of the upper crust. Large impacts excavate deeper layers, thereby exposing fresh material to the surface, but it is the small micrometeoroids that contribute ejecta, melt, and vapor on short timescales, including daily to yearly timescales. Photon-stimulated desorption (PSD) is important for the volatile elements, notably for the alkalis Na and K, and is a function of solar insolation and also of adsorbate coverage. PSD-derived vapor is of a much higher temperature than that from thermal desorption but is cooler than impact-derived vapor. Ion sputtering releases very energetic vapor, but the yield and velocity distribution of these ejecta are somewhat controversial. Sputtering yields depend strongly on the impacting ion species and its energy and impact angle, and will also depend on the grain size distribution, space weathering history, and composition of the regolith. Chemical sputtering relates to the production of ejecta through chemical reactions on the surface. Although it has been suggested as a source for Na and for water, little work has been done to determine rates for these chemical processes.

The relative importance of these processes can be constrained given the spatial and temporal distributions of the exospheric species to the extent that their source rates, velocity distributions, and forcing parameters are known. These topics are discussed in the following section.

15.2 OVERVIEW OF SOURCE AND LOSS PROCESSES

15.2.1 Source Processes

15.2.1.1 Thermal Desorption

Thermal desorption (or thermal evaporation) is the release of adsorbed atoms from a surface via heating. The process is related to the binding energy of the atom on the surface and to the vibrational frequency of this bound atom, such that the rate of thermal desorption is given by

$$R_{TD} = \nu_{TD}\, C \exp\left(-\frac{U}{kT_S}\right), \tag{15.1}$$

where ν_{TD}, the vibrational frequency of the atom on the surface, is commonly approximated as the ratio of the spacing between adsorption sites to the mean thermal speed of an adsorbed atom. U is the binding energy with the surface, k is the Boltzmann constant, C is the concentration of the desorbing species on the

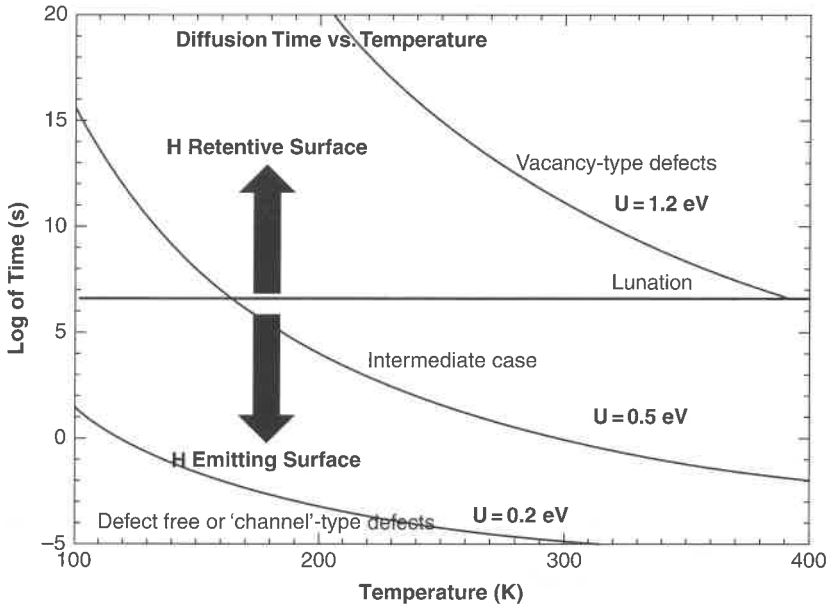

Figure 15.1. Diffusion time as a function of temperature for a family of binding energies, U, for H implanted at a depth of 100 nm onto a crystal with and without channel-type defects. This figure is illustrative of the effect of binding energy on release of volatiles, whereby an intermediate binding energy will result in highly temperature-dependent release or release dependent on plasma bombardment (solar wind on the dayside or magnetospheric effects on the nightside). High binding energy results in retentive surfaces, whereas low binding energy results in an emitting surface. From Farrell et al. (2015), with permission.

surface, and T_S is the surface temperature (e.g., Hunten et al., 1988). The vibrational frequency is often set at 10^{13} s^{-1} (Yakshinskiy et al., 2000), although Killen et al. (2007) argued that it might be several orders of magnitude smaller, following the arguments of Holmlid (2006). Leblanc and Johnson (2003) considered a Gaussian distribution of binding sites between 1.4 and 2.7 eV with a most probable value of 1.85 eV. After a number of vibrations on the order of $\exp(U/kT)$, where T is the absolute temperature, the atom is likely to escape the potential well. Thus the amount of time the atom spends in the adsorbed state is minuscule for small adsorption energies. Any process that contributes adsorbed atoms to the surface will contribute to a surface reservoir. The retention time on the surface is an exponential function of binding energy. Hunten and Sprague (1997, 2002) suggested that thermal desorption competes with PSD and sputtering, depleting the Na atoms in the surface layers of grains.

For sodium, thermal desorption produces atoms at only 0.03–0.05 eV energy (Yakshinskiy et al., 2000) compared with the escape energy of 2.07 eV. The energy distribution of atoms ejected by thermal desorption follows a Maxwell–Boltzmann flux distribution given by

$$f(E,\theta) = 2\cos\theta \frac{E}{(kT_s)^2} \exp\left(\frac{-E}{kT_s}\right), \tag{15.2}$$

where E is the energy of the ejecta and θ is the angle between the velocity vector of the ejecta and the normal to the surface.

No evidence for thermal desorption has been found for any of the species observed by the MESSENGER UVVS (e.g., Burger et al., 2012; Cassidy et al., 2015). This result is surprising in light of the predictions that thermal desorption should dominate near the subsolar point (Mura et al., 2009) and at aphelion (Leblanc et al., 2010). A possible explanation for the lack of observation of a thermal component is the observation that binding sites shift to higher energies after prolonged bombardment of the surface by 1-keV He^+ (Madey et al., 1998; Yakshinskiy et al., 2000) and, by analogy, by space weathering of an exposed surface. After one hour of bombardment by 1-keV He^+ ions, the thermal desorption of Na from SiO_2 shifts to temperatures near 1000 K (Madey et al., 1998). Bonding at defect sites (which increase with ion bombardment) is more important for wide-band-gap oxides (such as MgO) than for narrow-band-gap oxides (insulators such at TiO_2). Madey et al. (1998) also reported that the binding energy of alkalis increases with lower fractional coverage (<1 mono-layer). At higher coverage (>0.1 mono-layer), alkali bonding is influenced by cohesive interactions between the adsorbed atoms, which may decrease the adsorbate–substrate bond (Madey et al., 1998). The fractional coverage of atoms on surfaces affects thermal vaporization in such a way that atoms are less likely to desorb from surfaces when there is less than a mono-layer of coverage (Sneh et al., 1996).

If U [see equation (15.1)] increases with surface temperature, with lower fractional coverage, or with exposure to solar photons or ions, then the thermal desorption rate does not increase as fast with solar insolation as would be the case if U remained constant. Because the surface composition of Mercury is highly non-uniform, thermal desorption may be dependent not only on local solar time but also on the underlying mineralogy. Thus, thermal desorption is extremely complex and difficult to model accurately. Whether a surface is retentive or emitting of a particular volatile constituent depends strongly on the binding energy and temperature (Figure 15.1).

Thermally desorbed atoms ejected from the surface follow a Maxwellian flux distribution of the form

$$f(v) \propto v^3 \exp(-v^2/v_{th}^2), \tag{15.3}$$

where v is the neutral atom's velocity, $v_{th} = 2kT_S/m$ is the mean thermal speed, and m is the mass of the ejected neutral atom. The energy distribution of thermally desorbed Na atoms at 700 K is shown by the magenta line in Figure 15.2.

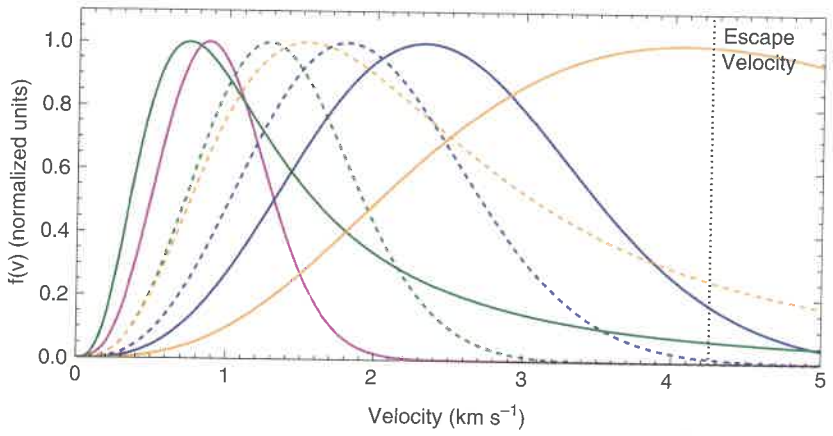

Figure 15.2. Velocity distributions for the major source processes expected for exospheric species: (1) magenta: Maxwellian at 700 K (thermal desorption); (2) dashed blue: Maxwellian at 3000 K (impact vaporization); (3) solid blue: Maxwellian at 5000 K (impact vaporization); (4) solid green: Weibull distribution used by Burger et al. (2010) for PSD; (5) dashed green: Maxwellian at 1500 K used by Leblanc et al. (2003) for PSD; (6) solid orange: sputter distribution with $U = 2$ eV used by Burger et al. (2010); (7) dashed broken orange: sputtering with $U = 0.28$ eV used by Leblanc et al. (2003).

The effectiveness of thermal desorption is influenced by surface diffusion between sites with different desorption energies (Farrell et al., 2015). The rate of transport of volatiles from grain interiors to the surface is governed by diffusion, grain size, grain composition, presence and thickness of a glassy rim, and grain lifetime at the regolith surface (Killen et al., 2004, 2007). For example, atoms diffuse to the surface of smaller grains more quickly than from larger grains, and thus small grains are depleted more rapidly in volatiles via thermal desorption (Killen et al., 2004). However, small grains also serve as a more efficient repository for adsorption of volatiles owing to their larger surface-to-volume ratio. Because the activation energy for diffusion is about one-tenth of the binding energy, surface diffusion – a mechanism whereby atoms can move along a surface – can result in atoms accessing deeper binding sites, where they are more stable against thermal vaporization, or becoming cold trapped underneath surface grains.

15.2.1.2 Impact Vaporization

Impact vaporization is the most universal process that promotes atomic species into the exosphere in that it is energetic enough to eject all species and for impact velocities > 5 km/s will probably vaporize all species rather than a select few. Mangano et al. (2007) concluded that micrometeoroid impact vaporization is the sole process continuously refilling the exosphere for Mg, Al, Si, S, Ca, and O. Impact vaporization has been variously described as a minor source for Na, delivering only a small percentage of the total source rate to Mercury's exosphere (Smyth and Marconi, 1995a, b), or a major source (Morgan et al., 1988; Borin et al., 2010), and so its importance remains somewhat uncertain. It is believed that impact vaporization is either the dominant or the exclusive process ejecting Ca, a refractory element, into the exosphere (Killen and Hahn, 2015). The moderately volatile species Mg shows temporal and spatial variation in its distribution and exospheric temperature suggestive of impact vaporization, as discussed below. Impacting particles of small sizes (<100 μm) constantly rain onto Mercury's surface at a mean velocity of ~20 km/s (Cintala, 1992), churning the regolith and vaporizing the surface. Larger meteoroids impact more sporadically, but with higher mean velocity and a double-peaked velocity distribution with peaks near 30 and 40 km/s (Mangano et al., 2007; Marchi et al., 2005). Many minor species that are refractory during vaporization of silicates in vacuum are highly volatile during hypervelocity impacts owing to the high temperatures and pressures (Gerasimov et al., 1999).

Impact events probe to a depth of several diameters of the impacting body and are therefore important in terms of supply of fresh grains to the surface, a process referred to as regolith gardening. This process is important in exposing fresh, unweathered material to the surface. Because meteoroid impacts probe much deeper than any process other than venting, and because the energy density of the process is very high, the exospheric products of this emission process most closely represent the surface composition as a whole. Mangano et al. (2007) performed simulations to analyze the effects in terms of the gaseous cloud produced by impacts of objects in the range 1 cm to 1 m. Particularly noticeable is the case of 10-cm meteoroids for which the enhancement, depending on the species considered, varies from one to four orders of magnitude over the mean exospheric background values.

Larger meteoroids will impact Mercury but at an unknown rate. Marchi et al. (2005) provided the distribution of impact probability as a function of impactor radius, up to objects of 100 m in radius. In particular, meteoroid impactors coming from the main asteroid belt are expected to impact on Mercury as well. The contribution by these larger meteoroids to the global mercurian exosphere is negligible on average; nevertheless, their impact is expected to produce strong, localized, but temporary increases in the exospheric density, enriched in material coming from deeper layers (Mangano et al., 2007). Mangano et al. (2007) calculated that a 1-m meteoroid impacting Mercury's dayside will produce an enhancement in the Na exosphere visible over the background at 400-km altitude for 800 s, and for 6000 s for the O exosphere. The nightside enhancements last longer relative to the background because the scale height of the background exosphere is lower. Although the impact frequency of such objects at Mercury is not negligible relative to the duration of the MESSENGER orbital mission phase (more than four years), they would be difficult to detect given their short lifetimes and localized effects.

Regardless of the size of the impactor, the initial ejecta from an impact will be high-temperature vapor (~3500–5000 K). This ejecta will quickly be followed by liquid + vapor at a slightly lower temperature (2500 K). The vapor ejected by cometary impacts may be hotter and include a large ionized component (Hornung et al., 2000; Kurosawa et al., 2010), followed quickly by thermalized vapor. In general, impact vapor may be much cooler than previously supposed because of rapid cooling. Energy distributions for Na produced by impact vaporization, defined by the Maxwellian flux speed distribution in equation (15.2), are shown in Figure 15.2 for vapor at $T = 3000$ K (dashed blue line) and $T = 5000$ K (solid blue line).

Soil grains melted by impact may subsequently release vapor as a result of the extreme temperatures (>2000°C) reached by some melts, giving off dissociated molecules, ions, and atoms into the vapor (Keller and McKay, 1997). This process places a portion of the silicate melt into vapor. Some of the vapor condenses on the rims of all soil grains, largely as amorphous glass rinds from 50 to 100 nm thick (McCord et al., 2011). Some of the charged ions neutralize, creating energetic atoms, such as the observed hot Ca and Mg (Killen, 2016).

Killen and Hahn (2015) showed that the source rate for calcium in the exosphere of Mercury can be produced by impact vaporization of interplanetary dust, fine grained micrometeoritic material which is believed to preferentially impinge on the dawn-side hemisphere – the ram direction (e.g., Janches et al., 2006). Dust ejection at the Moon was shown to be markedly concentrated in the ram direction by the results of the Lunar Atmosphere and Dust Environment Explorer (LADEE) Lunar Dust Experiment (Horanyi et al., 2015, 2016), lending further evidence that micrometeoroid dust impact is strongly asymmetric. A permanent, asymmetric dust cloud peaking near the dawn terminator was observed at the Moon and attributed to impacts by high-speed dust particles of cometary origin (Horanyi et al., 2015). This distribution is similar to the distribution of Ca in Mercury's exosphere. It is not known whether such a dust cloud exists at Mercury.

Seasonal variations seen in the planet-wide Ca emission rate (Burger et al., 2014) can be explained as Mercury traverses the interplanetary dust disk, given the relative inclination of the dust disk and Mercury's orbital plane of about 3.5°. One exception is near Mercury true anomaly angle (TAA) 25°–30°, where it has been shown that additional cometary dust from comet 2P/Encke is likely to encounter Mercury (Christou et al., 2015; Killen and Hahn, 2015).

The observed extreme temperature of the Ca exosphere (>50,000 K) (Burger et al., 2014) is more difficult to explain than the source rate. Killen (2016) attempted to outline possible processes that could produce these extreme temperatures, but more laboratory work is desirable to determine the excess energies of the various processes proposed.

15.2.1.3 Photon-Stimulated Desorption

Photon-stimulated desorption was first suggested as a source process for the Na exosphere of Mercury by McGrath and Johnson (1986). Photon-stimulated desorption results from an electron transfer induced by photon bombardment of the surface with energies greater than the threshold value of 3 to 4 eV. Fractional mono-layers of Na deposited on oxide surfaces adsorb as Na^+ (whereas multi-layers contain metallic Na). A photon can induce an electron transfer to an unoccupied Na^+ 3s level, neutralizing the adsorbed Na^+. This state is highly repulsive, but the Na atom thus created can either re-adsorb by charge transfer from the substrate or desorb from the surface, whichever process is faster. PSD acts only on adsorbed Na because photons do not penetrate the bulk of the solid.

A number of experiments have been performed to measure the cross sections for photon-stimulated desorption, electron-stimulated desorption, and ion-induced desorption for alkali elements (Madey et al., 1998; Yakshinskiy and Madey, 2004, 2005). The PSD cross section for Na desorption from SiO_2 films was measured by Yakshinskiy and Madey (2000) to be $\sim 3 \times 10^{-20}$ cm^2 for 5 eV photons. Burger et al. (2010) used a PSD cross section of 3×10^{-21} cm^2, taking into account porosity and temperature effects, and they set the photon-limited PSD rate to 2.7×10^8 cm^{-2} s^{-1} at the subsolar point during the first and second MESSENGER flybys. They argued that the PSD rate is everywhere diffusion-limited, consistent with the results of Killen et al. (2004). Burger al. (2010) found that a diffusion rate of 10^6–10^7 cm^{-2} s^{-1} is consistent with the data, depending on the sticking coefficient used, although this rate was increased by ion precipitation, which heats the surface and creates defects in the regolith lattice that allow diffusion to proceed more rapidly.

It was subsequently shown (Yakshinskiy and Madey, 2004) that the desorption cross section has an exponential dependence on the binding energy of a transient atom. If there are multiple adsorption sites on the surface for which the lifetimes are different, then the relative concentration in the higher-energy site increases. This behavior gives rise to PSD-inactive and PSD-active sites similar to the retentive and emitting surfaces shown in Figure 15.1. Either increased temperature or bombardment by high-energy ions or electrons can produce such a migration to high-energy sites, both of which are prevalent at Mercury. Sodium desorbs more easily from a wide-band-gap insulator such as glass than from a crystalline surface (Yakshinskiy and Madey, 2004). Glassy rims are expected to coat the surfaces of most grains on the surface of Mercury (Keller and McKay, 1997).

Mura (2012) pointed out that the loss rate of sodium particles from Mercury due to PSD release is a function of both TAA (heliocentric distance and velocity) and the assumed source velocity distribution. The energy distribution of these particles has been modeled with a Maxwell–Boltzmann flux distribution for a temperature of ~1200–1500 K (e.g., Leblanc and Johnson 2003),

$$f(E) = \frac{E}{kT} e^{(-E/kT)}, \tag{15.4}$$

and with a Weibull function (Johnson et al., 2002),

$$f(E) = x(1+x)\frac{E\beta^x}{(E+\beta)^{2+x}}, \tag{15.5}$$

where E is the energy of the emitted particle, T is the temperature of the distribution, x is a free parameter (assumed to be

0.7 by Mura), and β is the characteristic energy of the Weibull distribution. Burger and co-workers (Burger et al., 2010, 2012, 2014; Mouawad et al., 2011) also used a Weibull distribution with $x = 0.7$ but with β equal to the binding energy $U = 0.052$ eV and with the leading term, $x(1 + x)$, replaced with a normalization constant. The "fast" PSD velocity distribution of Burger et al. was taken from Johnson et al. (2002), who measured electron-stimulated desorption (ESD) of Na from amorphous ice. The Maxwellian velocity distribution at 1200 K was based on measurements by Yakshinskiy and Madey (1999) of Na ejected from SiO_2 by ESD. Yakshinskiy and Madey (2004) showed that the peak velocity of Na desorbing from a lunar sample by PSD is ~800 m/s (~900 K), less than that observed for desorption of Na from a SiO film (Yakshinskiy and Madey, 2000). A Maxwellian distribution for the velocity of Na ejected at 1500 K (dashed green line) and the Weibull distribution (solid green line) are shown in Figure 15.2.

Modeled fits to the rates of Na, K, and Mg ejected into the exosphere by PSD depend strongly on the assumed sticking probability and thermal accommodation coefficient. This is because if the atom sticks upon re-impact with the surface then a higher ejection rate is required to maintain the observed exosphere than would be needed if the atom bounces. Similarly, the mix of different processes derived from the models depends critically on the assumed thermal accommodation. If the thermal accommodation is assumed to be zero, or the sticking probability is unity, as in the models of Cassidy et al. (2015), the conclusion will be that PSD is the only ejection process because the exosphere is observed to have a characteristic temperature of ~1200 K, consistent with the presumed PSD velocity distribution. However, the sticking probability for Na measured by Yakshinskiy and Madey (2005) is 0.2–0.3 in the temperature range appropriate for Mercury's dayside. If the thermal accommodation coefficient is assumed to be 0.2 for Na, an admixture of at least 20% of impact vapor at a temperature of ~3000 K is required to maintain the observed exospheric temperature and also to populate the Na tail (Burger et al., 2010; Schmidt, 2012). With the smaller sticking probability, a smaller desorption cross section is required than for the sticking coefficient of unity assumed by Sarantos et al. (2012), because the atoms are reemitted. These reemitted atoms are not assumed to be "new" atoms in the models of Burger et al. (2012. 2014). According to Yakshinskiy and Madey (2005), potassium has a higher probability than Na of losing energy to substrate phonons and becoming trapped. The lack of temperature dependence in the sticking for K is an indication of a very efficient kinetic energy transfer to the substrate (i.e., K should be thermally accommodated to the surface) (Yakshinskiy and Madey, 2005). Presumably, the reverse is true for Na: a strong temperature dependence in sticking indicates that Na should not be thermally accommodated. This presumption seems to be confirmed by the observations: MESSENGER UVVS did not observe a thermal component in the Na exosphere.

15.2.1.4 Ion Sputtering

Ion sputtering results from the impinging of an ion of mass m_1 onto a surface; if the impact energy (E_i) is high enough, a new particle of mass m_2 may be extracted. Solar-wind protons (H^+) strike the lunar soil grains with enough energy to penetrate to depths of 5–10 nm (Starukhina and Shkuratov, 2000; Johnson, 1990). Grain rims are typically 50–100 nm thick (Noble et al., 2005), so the protons penetrate only the rim, not the crystalline grain, if the grains are coated with glass. Thus protons preferentially sputter from glassy rims, which may not have compositions consistent with the bulk regolith. Plagioclase rims on lunar grains analyzed by Keller and McKay (1997) are depleted in Al by 50% and depleted in Ca by 80% relative to their host grains; the orthopyroxene rim is depleted of Mg by 80% and enriched in O (presumed to be bound to H). Excess oxygen found in rims analyzed by Keller and McKay is approximately 12–15% by number in the rims of both orthopyroxene and plagioclase grains, presumably bound to H in the form of hydroxyl. On the other hand, these rims are enriched in Si, S, Fe, Al, and Ti relative to their host grains. The amorphous rims on cristobalite grains show compositions nearly identical to those of the host grains. The wide range in the chemical properties of amorphous grains relative to their host grains on the Moon means that most likely only impact vaporization produces ejecta reflective of the bulk composition of the regolith, and the sources from different regions must reflect different compositional terrains.

For light ions (e.g., H^+), ion sputtering is a two-step process: backscattering of the ion over a surface target, and ejection of a second surface atom by the backscattered ion; in most cases, the ejected particle is neutral (Hofer, 1991). The velocity function for neutral ejecta peaks at few eV (Sigmund, 1969; Sieveka and Johnson, 1984) and can be empirically reproduced by the following function:

$$f_s(E_e, T_m) = c_n \frac{E_e}{(E_e + E_b)^3}\left[1 - \left(\frac{E_e + E_b}{T_m}\right)^{1/2}\right], \qquad (15.6)$$

where E_b is the surface binding energy of the atomic species extracted, E_e the energy of the emitted particles, and c_n the normalization constant. For Na sputtered by H, T_m is given by (e.g., Mura et al., 2009)

$$T_m = E_i \frac{4 m_H m_{Na}}{(m_H + m_{Na})^2}. \qquad (15.7)$$

In this context E_b is the chemisorption energy and E_i is the energy of the incoming proton. Although the binding energy for Na has sometimes been taken to be ~2 eV (McGrath et al., 1986), Yakshinskiy et al. (2000) reported that their measurements are consistent with multiple binding sites between 1.4 and 2.7 eV, with a most probable value of 1.85 eV. Consequently, Leblanc and Johnson (2003) used a Gaussian distribution for E_b with the most probable value equal to 1.85 eV. The sputtered Na energy distribution with $U = 2$ eV is shown in Figure 15.2 (solid orange line). For heavy ions, the ion impact direction does not affect the angular distribution of ejecta, which is a $\cos^n(\alpha)$ function, where α is the angle from the surface normal direction and n is usually between 1 and 2 (note that this function has never been measured on powdered surfaces). For light ions, the angular distribution is related to the ion impact direction and exhibits a maximum close to the mirror angle, where the angle

of ejection equals the angle of incidence along the incoming direction of the ion. The resulting neutral differential flux is

$$\frac{d\Phi_n}{dE_e} = cY\int_{E_{min}}^{E_{max}} \frac{d\Phi_i}{dE_i} f_s(E_e, E_i)dE_i, \quad (15.8)$$

where Y is the process yield, c is the surface relative abundance of the atomic species considered, Φ_i is the ion flux, f_s is the distribution function of ejection energy, E_e is the energy of the emitted particle and is related to E_b, the surface binding energy (Mura et al., 2007), and E_i is the energy of the incoming ion. The yield reduction due to regolith porosity (Cassidy and Johnson, 2005) is expected to be about one-third and is not considered in equation (15.8). Also not considered in equation (15.8) are the energy dependence of the yield and the angular distribution of emitted particles.

A fraction of atoms and ions sputtered from the surface are ejected in excited states, which will decay by radiative transitions. These excited states decay within millimeters of the surface and are therefore not taken into account in analysis of remote observations of exospheric emission (Dzioba and Kelly, 1980).

15.2.1.5 Chemical Sputtering

Chemical sputtering relates to the release of atoms and molecules from regolith grains during chemical reactions between implanted solar-wind or magnetospheric ions (predominantly implanted protons) and regolith material. The radiolytic processes leading to chemical sputtering consist of several steps: implantation of reactive ions, followed by chemical reactions with target atoms or molecules, and, finally, desorption of the reaction products (Roth, 1983).

Chemical sputtering may produce and remove elemental sodium (Potter, 1995), hydrogen, hydroxyl, and water (e.g., Crider and Vondrak, 2003) from the surface to the exosphere. Mura et al. (2009) argued that chemical sputtering does not eject Na atoms directly but liberates them for another process, such as PSD, to eject them from the surface. In this sense, chemical sputtering is similar to the ion-enhanced diffusion proposed by Burger et al. (2010) to explain the increase in PSD rate in regions open to solar-wind ion precipitation. This process deserves further study.

15.2.1.6 Gas–Surface Interaction

All processes discussed here are affected by gas–surface interactions, which are functions of surface composition and space weathering effects. As discussed earlier, thermal accommodation, sticking probabilities, crystal defects and binding sites, and grain structures such as agglutinates and glassy rims all contribute. Interactions with the surface are described in terms of adsorption and sticking, which we will discuss here.

Sticking is a term that relates to the fraction of atoms impinging onto a surface that are retained. When a surface is sufficiently cold, the sticking fraction can be approximated by unity, so that every atom hitting the surface is retained, either by chemisorption (bonding with the surface), or physisorption by van der Waals interactions. With the exception of H and He, returning particles essentially stick with a residence time that depends on the surface temperature and the availability of deep sites (Smith and Kay, 1997; Yakshinskiy et al., 2000). In laboratory studies a distinction can be made between direct reflection, sticking–migration–desorption, and sticking and becoming bound in a deep well (Smith and Kay, 1997). In modeling, one typically uses a net sticking coefficient, S, which combines the probability of physisorption and the probability of finding a binding site. Yakshinskiy et al. (2000) gave the net sticking probability for Na on a silicate: $S \sim 0.5$ at 250 K, decreasing to 0.2 at 500 K. However, as demonstrated for water on lunar materials, the sticking coefficient and adsorption probabilities are highly dependent not only on composition but also on the physical state of the surface and the weathering history (Poston et al., 2015). Scanning electron microscope (SEM) images of typical lunar agglutinates extracted from Apollo soil samples show that the glassy surface is extensively coated with small, fine-grained soil fragments. These images demonstrate the irregular shapes and delicate structures common to agglutinates. Visible on the surface of these agglutinates are regions of glassy, fragment-free surfaces adjacent to fragment-laden surfaces. The texture of the grain surface, composed of a coating of tightly welded fine-fragment material, will affect desorption and sequestration (Domingue et al., 2014). The surface area of the grains is very important in determining the adsorptive efficiency, so small grains can be highly adsorptive.

Adsorption is a term that encompasses both physisorption and chemisorption, which are in fact very different interactions. As mentioned above, physisorption involves the van der Waals potential, thus is electrostatic in nature and related to the creation of induced dipole moments at the surface. A physisorbed atom can be desorbed by thermally exciting internal states or a surface state (Madey et al., 2002). Exciting a surface state can lead to ejection of an atom or molecule, whereas excitation of the internal states leads to ejection of an atom only if it is pointing outward from the surface.

If the atom is not reflected, any atom returning to the surface likely remains in a physisorbed state a very short time before finding a binding site through surface diffusion. That is, the returning atoms or molecules initially become weakly adsorbed on the surface. In this state they can either migrate along the surface of a grain until they find a deep adsorption site (characterized by chemisorption) or they can desorb thermally. In order to desorb, an activation energy greater than the difference between the bound potential and the surface potential must be available. The activation energy can be obtained by a thermal or photon process.

Once an atom finds a deep potential well it becomes chemisorbed, characterized by chemical bonding. The depth of the bonding sites depends on the particular physical state of the surface. Chemisorption sites extend over a wide range with a distribution of adsorption energies characterized by a Weibull distribution. This phenomenon has been studied extensively for water by temperature-programmed desorption (TPD) (e.g., Poston et al., 2015). An important finding is that the adsorption energy – or more properly the distribution of binding sites – is highly dependent on the composition of the surface, the grain sizes, and the weathering history. For instance, mature

anorthositic lunar soil has a distribution of binding sites for water that peaks at about 0.7 eV and extends to 1.5 eV, whereas sub-mature low-titanium basalt has binding energies extending only to about 0.6 eV.

Description of chemisorption in terms of the usual energy–distance curve is an oversimplification because more coordinates are needed. Binding energies depend not only also on the coordinate along the surface (e.g., top site versus hollow site) but also on the interatomic distance in the precursor molecule, its orientation with respect to the surface, and the individual coordinates of the dissociation products. Thus, the problem of obtaining the relevant energies for the chemisorption process is extremely complicated.

An additional factor is surface charging. Dayside excitation by solar ultraviolet (UV) and X-rays causes the photoemission of electrons from surface grains, creating a positive potential (Farrell et al., 2007). The surfaces of grains can be oppositely charged by photon and electron fluxes (Jurac et al., 1995) affecting the amount of adsorbate available for desorption. Proton bombardment can result in positive charging and, therefore, inward sodium diffusion, whereas low-energy electrons can cause negative charging and, therefore, outward diffusion of sodium (Madey et al., 2002). The magnitude of the effect is at present poorly constrained by laboratory measurements.

15.2.1.7 Synopsis of Source Processes

Despite continued measurements needed for accurate models (e.g., the PSD cross sections), the actual relative mix of source processes has remained ambiguous, partly because of uncertainties in the velocity distributions, thermal accommodation, and sticking coefficients of the atoms when they interact with the surface. Estimates of removal by PSD of Na and K made by Wurz et al. (2010) indicated that this process dominates by about three orders of magnitude over either micrometeoroid impact vaporization or physical sputtering. Other simulation studies, however, have suggested that impact vaporization is a significant contributor, ranging from about 20% of that for PSD for Na (Burger et al., 2010; Mouawad et al., 2011) to all the exospheric Na produced via impact vaporization (Morgan et al., 1988; Borin et al., 2010). The Na production rate due to impact vaporization required to populate the tail in the models of Schmidt et al. (2012) – 1.8×10^6 atoms cm^{-2} s^{-1} for a 5000 K velocity distribution – is matched by the impact vaporization rate given by Burger et al. (2010) scaled to the Na wt% measured by MESSENGER.

15.2.2 Loss Processes

Neutral species in Mercury's exosphere are lost by collisions with the surface, gravitational escape (i.e., reaching the Hill sphere), or photoionization, the process by which solar photons remove electrons from neutral atoms and create pickup ions that are governed by electrodynamic forces rather than gravitational forces. About 85% of photoionized species are estimated to be entrained in the solar wind and lost from Mercury (e.g., Leblanc et al., 2003). Radiation pressure can accelerate atoms to above the escape velocity that otherwise would not escape. These processes are discussed below.

15.2.2.1 Radiation Pressure Effects

The constituents in Mercury's exosphere are subjected to radiation acceleration which pushes neutral species anti-sunward, forming a comet-like tail behind Mercury. Radiation acceleration is a consequence of the resonant-scattering emission process. Solar photons with a single incident direction are absorbed at the resonant wavelength (e.g., the Na D_1 and D_2 lines at 589.7 nm and 589.1 nm in the Na atom's rest frame) and nearly instantly reemitted approximately isotropically. Because photons have finite momentum, the atom experiences an impulse equal to the momentum difference between the incident and scattered photons. The magnitude of the radiation acceleration depends on the solar flux at the Doppler-shifted wavelength in the atom's rest frame. Because of deep Fraunhofer absorption lines in the solar spectrum, the photon flux experienced by an atom is a strong function of its radial velocity relative to the Sun. The magnitude of the radiation acceleration a_{rad} was given approximately by Smyth (1983):

$$a_{rad} = \sum_i \frac{h}{m\lambda_i} g_i, \tag{15.9}$$

where h is Planck's constant, m is the mass of the scattering atom, λ is the resonant wavelength, and g is the g-value of the transition (the product of the photon flux at the transition and the scattering probability per atom). The acceleration is the sum over all resonant transitions, i, but in practice only the strongest transitions need to be considered. The g-values for important transitions of species predicted to be in Mercury's exosphere were compiled by Killen et al. (2009).

The magnitude of the radiation acceleration as a function of Mercury true anomaly angle is shown for Na, Ca, and Mg atoms at rest relative to Mercury in Figure 15.3. Radiation acceleration has the greatest effect on the motion of Na atoms and is not much of a factor when determining the motion of Mg atoms because of weak absorptions. For Ca, the trajectories are

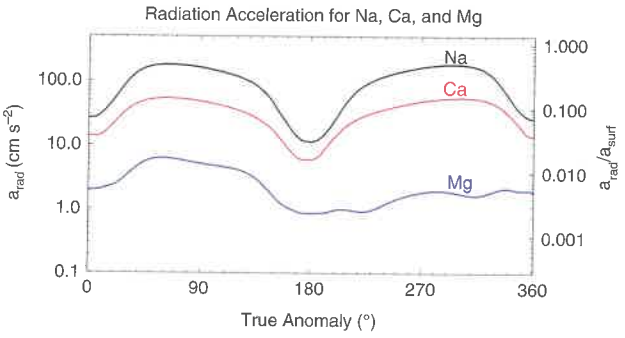

Figure 15.3. Acceleration due to radiation pressure is shown in absolute units (cm s^{-2}) for Na (black), Ca (red), and Mg (blue) at rest relative to Mercury (left axis) and as a fraction of gravitational acceleration at the surface (right axis). The magnitude of radiation acceleration (a_{rad}) depends on the true anomaly because of Mercury's changing heliocentric distance and the variation in Doppler shift of the relevant transitions. Deep Fraunhofer features contribute to the strongly varying radiation pressure of Na and Ca versus true anomaly. Acceleration due to radiation pressure for Na approaches 50% of surface gravitational acceleration and remains high except near aphelion and perihelion.

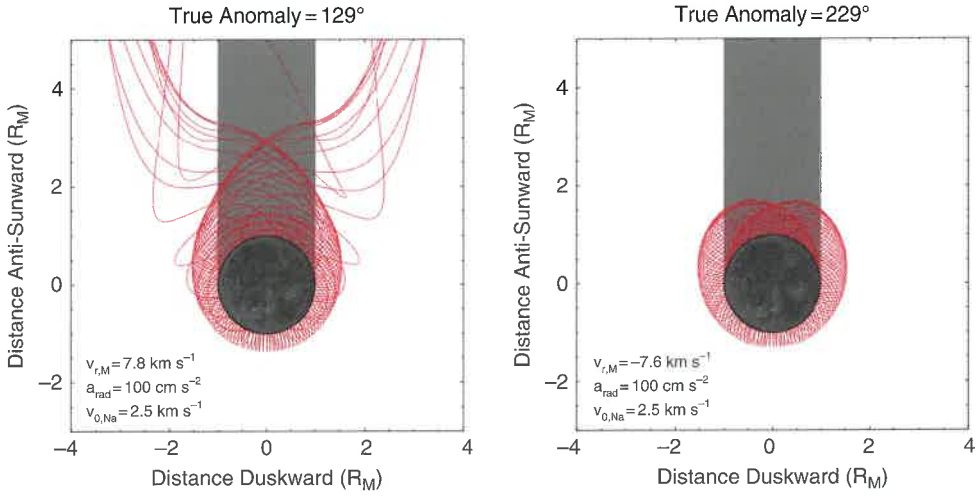

Figure 15.4. Comparison of Na trajectories ejected from Mercury at two true anomalies when the initial radiation acceleration is the same but the direction of Mercury's radial motion relative to the Sun is different. The Sun is downward in this representation, and Mercury's shadow is shown by the gray region extending upward. Na atoms experience no radiation acceleration while in Mercury's shadow. Na atoms are ejected radially outward from Mercury with an initial speed with respect to Mercury of $v_{0,Na} = 2.5$ km s^{-1}. The radiation acceleration for each case is 100 cm s^{-2}, but the left panel is during Mercury's outbound phase (TAA = 129°) with Mercury's distance from the Sun increasing (radial velocity $v_{r,M} = 7.8$ km s^{-1}), and the left panel is during the inbound phase (TAA = 229°) with Mercury's distance decreasing ($v_{r,M} = -7.6$ km s^{-1}).

affected, although the short photoionization lifetime (discussed below) results in a large fraction of Ca atoms being photoionized before radiation acceleration effects become significant.

Potter et al. (2007) showed that radiation acceleration affects the trajectories of Na atoms differently, for the same initial magnitude of radiation acceleration, at different parts of Mercury's orbit. On the outbound portion of Mercury's orbit (0° < TAA < 180°, when Mercury's distance from the Sun is increasing), there is positive feedback such that the radiation acceleration of Na atoms increases as their heliocentric radial velocity increases. On the inbound portion of the orbit where heliocentric velocity is negative (180° < TAA < 360°), the opposite occurs: there is negative feedback that retards the heliocentric acceleration of the Na atoms. These feedback effects occur because of the deep solar Fraunhofer lines that dominate the shape of the solar spectrum around the wavelengths of Na D transitions. In general, a_{rad} increases with the magnitude of the radial velocity toward or away from the Sun. During the outbound leg, Na atoms at rest with respect to Mercury have a net positive radial velocity relative to the Sun (i.e., they are moving away from the Sun). Radiation acceleration is in the same direction as the atom's initial motion, so the radial velocity increases, which in turn increases the radiation acceleration, resulting in positive feedback. During the inbound leg, Na atoms at rest with respect to the planet are moving with a net speed toward the Sun (a negative radial velocity). The radiation acceleration is directed in the opposite direction so the atom's speed toward the Sun decreases, decreasing the radiation acceleration and setting up negative feedback. This pattern is illustrated in Figure 15.4, which shows the trajectories of Na atoms at times when a_{rad} for an atom at rest relative to Mercury is the same but Mercury's radial velocity relative to the Sun is in opposite directions. It can be seen that it is easier for atoms to escape down the tail on the outbound leg (left panel) than the inbound leg (right panel) for atoms ejected well below Mercury's escape velocity (4.25 km s^{-1}).

15.2.2.2 Photoionization

Because photoionization rates depend on the incident solar flux at Mercury, they are a strong function of Mercury true anomaly angle and slightly dependent on the solar cycle. Photoionization lifetimes (the inverse of the photoionization rate) for Na, Ca, and Mg over the course of a Mercury year are given in Figure 15.5; these lifetimes are based on rates at 1 AU presented by Huebner et al. (1992) and Huebner and Mukherjee (2015). It can be seen that Mg has the longest lifetime, up to 100 h, whereas Ca has the shortest, with a lifetime under an hour.

There are uncertainties in the exact photoionization lifetime for each species. Huebner et al. (1992) presented two significantly different values for the photoionization rates of Na based on experimental (red line in Figure 15.5a) and theoretical (black line) cross sections, with a preference toward the theoretical cross section. Although both sets of cross sections have been used in Mercury models (e.g., Leblanc et al., 2003; Burger et al., 2010), calculations by Combi et al. (1997) and observations of the comet Hale–Bopp Na tail by Cremonese et al. (1997) were both consistent with the theoretical value published by Huebner et al. (1992) [see Killen et al. (2007) for further discussion]. More recently, Huebner and Mukherjee (2015) published an updated photoionization rate for Na using cross sections from two databases from Verner and coworkers (Verner et al., 1993, 1996; Verner and Yakovlev, 1995) and TOPbase (http://cdsweb.u-strasbg.fr/topbase/xsections.html). The new cross sections imply a ~20% adjustment in the Na ionization rate compared with the theoretical value given by Huebner et al. (1992).

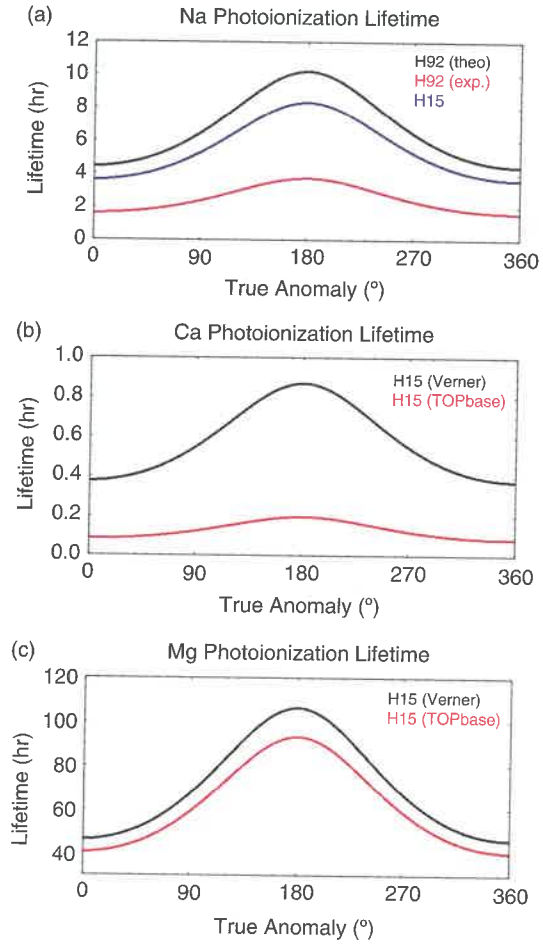

Figure 15.5. Photoionization lifetimes as a function of true anomaly angle for (a) Na, (b) Ca, and (c) Mg. References: H92: Huebner et al. (1992); H15: Huebner and Mukherjee (2015). For Na, Huebner et al. (1992) gave theoretical and experimental values for the cross section. Huebner and Mukherjee (2015) gave cross sections from two groups: Verner and co-workers (Verner et al., 1993, 1996; Verner and Yakovlev, 1995), and TOPbase. See text for further discussion.

The Ca photoionization rate is even more uncertain. From a pre-publication personal communication from W. Huebner to R. M. Killen, Burger et al. (2012, 2014) used the ionization rate associated with Verner and co-workers in Huebner and Mukherjee (2015) (black line in Figure 15.5b). Huebner and Mukherjee (2015) favored the value from TOPbase (red) as Verner and co-workers had smoothed over resonances near the threshold energy. This TOPbase ionization rate is 4.4 times the Verner rate. Had Burger et al. (2014) used this more recent value, they would have required a significantly higher temperature for the Ca than the 70,000 K their model required, possibly as high as >150,000 K. Unfortunately, the uncertainties in the cross sections are unclear from Huebner et al. (1992). The Mg ionization rate also shows a discrepancy between the two databases used by Huebner and Mukherjee (2015), although it is only ~15%.

15.2.2.3 Kinetic Escape

An atom will escape from the gravity well of a planetary body when its velocity exceeds the escape velocity:

$$v_{esc} = \left(\frac{2GM}{r}\right)^{1/2}, \tag{15.10}$$

where G is the gravitational constant, M is the mass of the planet, and r is the radial distance from the planet center. Because the escape velocity decreases as the distance from the planet center increases, the rate of Jeans escape (atom cm^{-2} s^{-1}), the escape from a planetary atmosphere by thermal evaporation, depends on the exobase distance. Jeans escape is derived for thermal escape from a planetary atmosphere and is thus not strictly applicable to a surface-bounded exosphere, but the formulation is sometimes used as an approximation. The velocity distribution is assumed to be Maxwellian. The Jeans flux is given by

$$F_{Jeans}(r) = \frac{N(r)v_m}{2\pi^{1/2}} e^{-\lambda}(\lambda + 1), \tag{15.11}$$

where v_m is the most probable velocity of a Maxwellian distribution,

$$v_m = \left(\frac{2kT}{m}\right)^{1/2}, \tag{15.12}$$

T is the temperature, m is the atomic mass, $N(r)$ is the number density at radius r, and λ is given by

$$\lambda = \frac{v_{esc}^2}{v_m^2} = \frac{GMm}{rkT}, \tag{15.13}$$

and is generally referred to as the escape parameter (essentially the gravitational potential energy in units of kT). It is useful to look at gravitational escape as a function of planetary mass, temperature, and mass of the atomic species as shown in Figure 15.6.

Even for water, the fraction of released vapor that escapes at 3000 K is less than 25% on the initial trajectory. Therefore, for metals (Na, Mg), escape or permanent loss is expected to result from photoionization or some process that produces a very hot vapor, such as sputtering or the high-velocity tail of the impact vapor. For Na, radiation pressure enhances escape at some true anomaly angles, but radiation pressure is insignificant for Mg. Nevertheless escaping Mg has been observed at Mercury, which necessitates an energetic source process. The extreme temperature of the Ca exosphere (Burger et al., 2014) implies that the Ca is escaping; however, there may be an unobserved molecular component that condenses back to the surface (Killen, 2015).

15.3 MESSENGER OBSERVATIONS AND MODELS

15.3.1 Sodium

The sodium tail – the component of the exosphere that is escaping anti-sunward primarily due to radiation-pressure-induced acceleration and first imaged by Potter et al. (2002) – was imaged by UVVS during each of MESSENGER's three

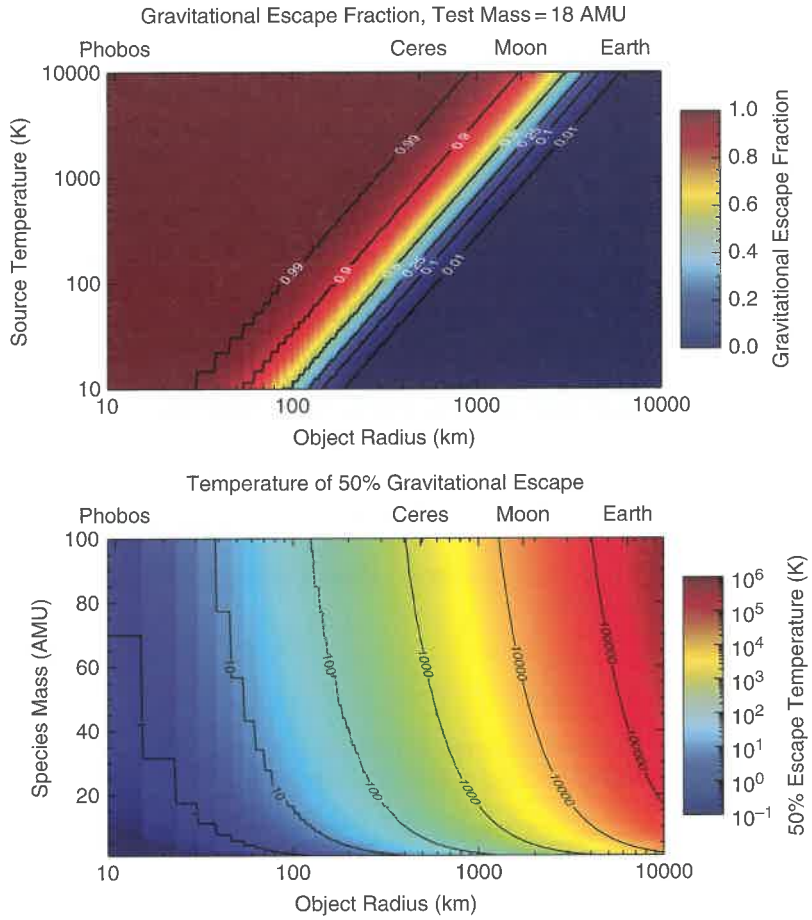

Figure 15.6. (a) The gravitational escape fraction for a test mass of 18 AMU (color coded) as a function of source temperature and object radius, for a bulk density of 3 g cm^{-3}. It can be seen that water is either completely lost or retained except for a narrow band as a function of source temperature and object size (or equivalently mass). (b) The source temperature (color coded) for 50% gravitational escape for species mass (AMU) versus object radius, for a bulk density of 3 g cm^{-3} (adapted from Killen et al., 2014). For Mercury, with a radius of 2439 km, the temperature for 50% gravitational escape probability is above that expected for impact vaporization temperatures (~3000 K) or photon-stimulated desorption (1200 K) for all species except H, H_2, He, OH, and H_2O.

Mercury flybys. The tail exhibited a nearly uniform north–south emission strength during the first and second flybys (Burger et al., 2010). Scaled to the same levels, the tail was practically non-existent during the third flyby. Although the radiation pressure for an atom at rest with respect to Mercury is near its peak for TAA 292° and only beginning to decrease for TAA 326° (see Figure 15.3), there is a negative feedback in the radiation pressure for true anomaly angles >180° such that the effective radiation pressure at TAA 326° is quite weak (e.g., Potter et al., 2007; Cassidy et al., 2015). UVVS observations of the sodium tail confirm the seasonal variation expected from the radiation pressure (Figure 15.7).

McClintock et al. (2009) used a Monte Carlo model (see Burger et al., 2010) to demonstrate that the Na observed during the second MESSENGER flyby was not consistent with a spherically symmetric source of Na but instead showed a northern enhancement. On the third flyby there was no apparent northern enhancement in Na relative to east or west, and only a very slight excess of Na over the south pole relative to the north pole (Vervack et al., 2010). This pattern is in contrast to the large excesses in both Ca and Mg over the north pole relative to the south pole during the third flyby, indicating very different source processes. High-latitude enhancement in the Na surface content (Peplowski et al., 2014) must be considered in future simulations of the Na exosphere, especially for models at high latitudes for which the Na content of the regolith is double that at the equator.

The observations during the orbital phase of MESSENGER were of several general types, termed dayside limb scans, nightside tail sweeps, ride-alongs, and stares. Because of orbital constraints, most of the limb scans have tangent points near the equator or at low latitudes (Figure 14.9). Notable exceptions are the limb scans approximately perpendicular to the spin axis at the south pole. In spite of limited spatial coverage, the UVVS provided unprecedented spatial resolution and observation cadence for more than 16 Mercury years of near-daily observations.

The UVVS observations analyzed by Cassidy et al. (2015) showed year-to-year repeatability: at a given local time and TAA the emissions were nearly identical from one Mercury year to the next. Cassidy et al. (2015) interpreted the UVVS Na limb scan data with a simple model to estimate the temperature and density of the near-surface exosphere within approximately 50–1500 km of the surface. The model accounts for the effects of radiation acceleration and includes single scattering with a uniform phase function. Cassidy et al. (2015) derived a temperature of ~1200 K with some local-time variation (Figure 15.8), including observations over the south polar region. They found that the tangent column density at 300 km above the subsolar point was a factor of 3 higher at aphelion than at perihelion. This difference may be accounted for by the fact that radiation pressure reduces the scale height at perihelion, so this measurement does not give a direct comparison with total abundance. Ground-based observations taken over

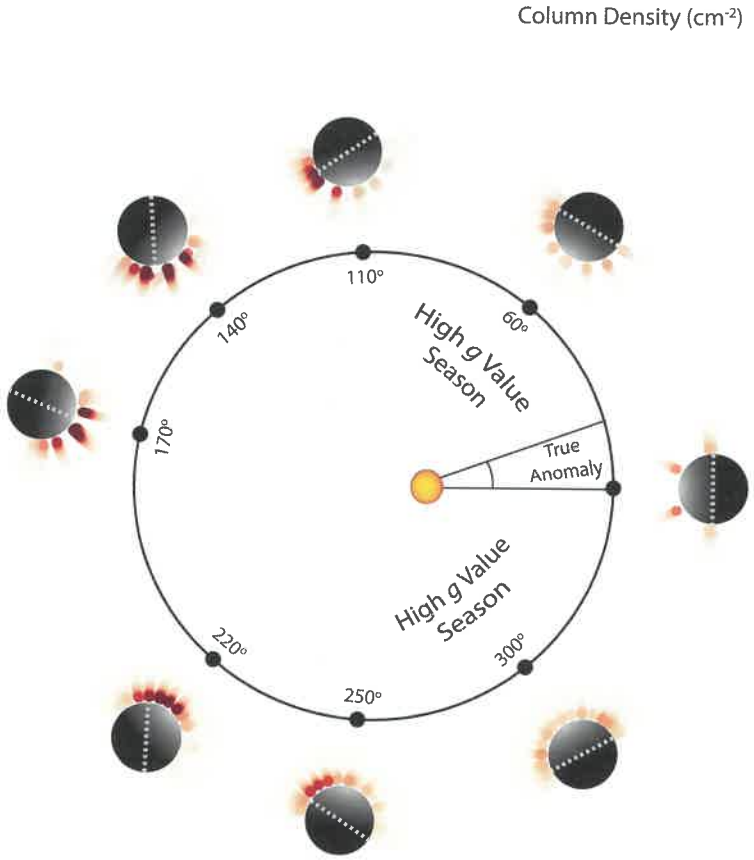

Figure 15.7. Illustration of "seasonal" variations in Mercury's exospheric emission. Observations of Mercury's sodium tail were taken at the indicated true anomalies. Compare with Figure 15.3 for radiation pressure. Note that the shadow region anti-sunward of Mercury prevents resonant emission, so the "streamers" are not related to density. The emission scales as the inverse square of heliocentric distance, so the column abundance scales as the product of the emission and the squared heliocentric distance, a factor of 2.3 increase from aphelion to perihelion.

a period of seven years reported by Potter et al. (2007) showed on average about the same disk-averaged column abundance at aphelion and perihelion, but with a spread of a factor of 3 at aphelion and a much smaller spread at perihelion. These results suggest that photon-stimulated desorption is the primary source process. However, a high-energy process must also be present to produce both seasonal and episodically variable effects seen especially in ground-based data, and to populate the tail (Schmidt, 2012). Vaporization by micrometeoroid impact has been shown to be seasonally repeatable (Killen and Hahn, 2015) and thus represents a seasonal high-energy source that can potentially populate the tail. Impacts by larger meteoroids are rare, and the effects are short-lived (Mangano et al., 2007). Sputtering would produce a high-energy, episodically variable component, but observations of ion sputtering by the UVVS instrument were precluded by instrument noise produced by high-energy charged particles, especially during solar energetic particle (SEP) events.

Given that impact vaporization is almost certainly the most important source of the calcium exosphere (see Section 15.3.2; Killen and Hahn, 2015), it must play a role in imparting Na to the exosphere as well. The Na content, as well as that of most of the other species seen in the exosphere, is spatially variable in the surface grains (Peplowski et al., 2014), ranging from 2.8 wt% at low northern latitudes (0°–15° N) to 4.9 wt% at high northern latitudes (80°–90°N). Given an average Na surface concentration of 2.8 wt%, and the impact vaporization rate from Cintala (1992), the Na impact vaporization rate should be 1.0×10^6 cm^{-2} s^{-1} at aphelion and 2.4×10^6 cm^{-2} s^{-1} at perihelion, corresponding to global rates of 7.5×10^{23} s^{-1} at aphelion to 1.8×10^{24} s^{-1} at perihelion. These values represent 4% of the rate needed to populate the exosphere for a one-bounce model (i.e., the atoms stick on re-contact with the surface) or all of the required rate if the lifetime is the photoionization lifetime (i.e., the atoms do not stick on re-contact with the surface). Assumptions concerning the gas–surface interaction are therefore critical to conclusions concerning the importance of the various source processes. In addition, pre-MESENGER models all used lunar composition and their results must be scaled. For instance, Mouawad et al. (2011) assumed a Na fraction of 0.5 wt% (i.e., a lunar composition) in deriving a Na impact vaporization rate of 3.5×10^5 cm^{-2} s^{-1}, but they gave an upper limit on the impact vaporization rate from observational data of 2.1×10^6 cm^{-2} s^{-1}, consistent with the impact vaporization rate that would be derived if scaled to MESSENGER surface composition measurements. If the total PSD desorption rate is 3.5×10^{24} s^{-1} (Burger et al., 2010) and the total impact vaporization rate is 1.8×10^{24} s^{-1}, then impact vaporization represents about 35% of the total ejection of Na at Mercury rather than the 2% estimated by Mouawad et al. (2011) on the basis of an assumed lunar composition. If this is the case, then some thermal accommodation must be taking place to maintain the exosphere at 1200–1400 K.

A PSD desorption rate of 3.5×10^{24} s^{-1} was derived by Burger et al. (2010) from the PSD cross section of

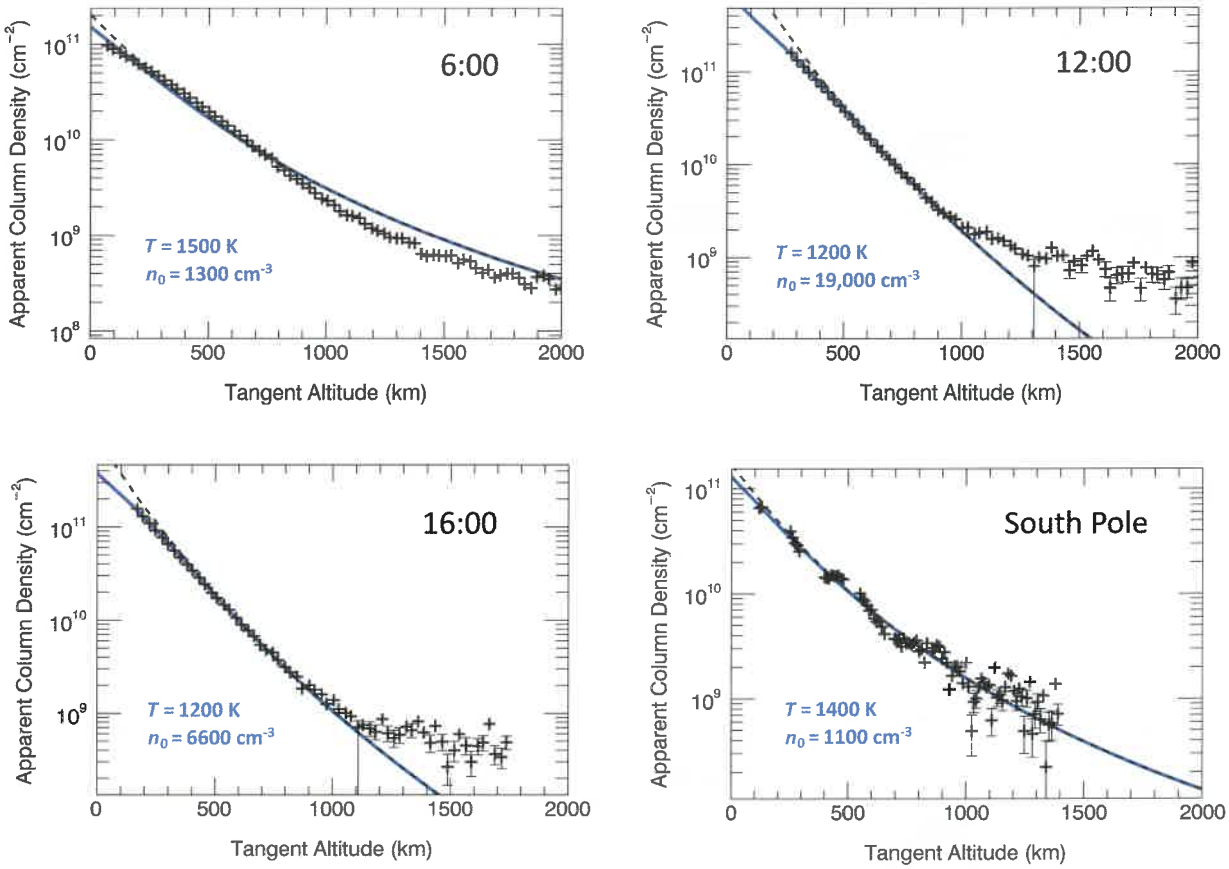

Figure 15.8. Examples of fits to near-equatorial dayside limb scans (local times indicated) and the south pole observations for Na (Cassidy et al., 2015). Only the low-altitude component of the profile was fit. Data are represented by crosses, and the fit is shown by a black dashed line. The blue line is a Chamberlain fit with the optical depth correction. The resulting temperature and surface density used for the fits are indicated by blue text. Observations were taken on 6 June 2012, except for the south pole observation, which took place on 17 October 2011.

Yakshinskiy and Madey (1999), 3×10^{-21} cm^2, and a total surface number density of 7.5×10^{14} cm^{-2} for the first two MESSENGER flybys at a heliocentric distance of 0.35 AU. However, Burger et al. (2010) assumed a lunar abundance of Na, 0.5 wt%, and a surface density of 7.5×10^{14} cm^{-2}. Scaling the PSD source rate to the measured Na wt% would imply a PSD desorption rate of ~1.9×10^{25} s^{-1}.

The simulation of Schmidt (2012) yielded a total source rate from impact vaporization in the range 1.8×10^6 to 3.6×10^6 cm^{-2} s^{-1} Na atoms in order to obtain the Na escape rate required to match the tail observations, given that the escape is due to an impact vaporization source. Because the Burger (2010) impact vaporization rate was derived from first principles for a lunar composition (Na wt% = 0.5), scaling that figure by a factor of 5.6 to the Na mass fraction observed by MESSENGER (Na wt% = 2.8) would give an impact vaporization rate of 2×10^6 Na atoms cm^{-2} s^{-1}, consistent with the Schmidt (2012) rate derived by matching the observed Na escaping down the tail.

Mura (2012) found that for a Weibull distribution of velocities (their "fast" distribution) for PSD, up to one-third of the sodium particles escape if the characteristic energy β = 0.086 eV, whereas for the Maxwellian case the loss rate is smaller by a factor of 3 but still accounts for 10% of the source. Thus, the high-velocity portion of the PSD source distribution can populate Mercury's tail if a high-energy tail to the distribution is assumed. Schmidt et al. (2012) also performed three-dimensional time-dependent modeling of Mercury's extended sodium tail, considering the effects of orbital motion, gas–surface interaction, variable source rates, and spatially non-uniform distributions of the sources (see Section 15.2.1). They concluded that either a combination of a slow impact vaporization source (3000 K) and a "fast" PSD source or a combination of a slow PSD source and a fast (5000 K) impact vaporization source can result in a ~20% loss of the released Na atoms down the tail, depending on orbital phase. They estimated that a loss rate of ~10^{24} Na atoms s^{-1} is required to populate the tail on average, and that a sputter source can supply at most 25% of this required rate except in exceptional circumstances.

If the average loss rate of Na atoms is 3.5×10^{23} Na atoms s^{-1}, as derived by Leblanc and Johnson (2003), this average represents a loss rate of 26% of the impact vaporization source. Schmidt et al. (2012) estimated that about 15% of the atoms derived from a slow impact vaporization source or 30% of those from a fast impact vaporization source would escape. Thus the derived loss rate is closer to the fast impact vaporization loss rate than the slow rate, but a combination of impact vaporization and PSD would also fit the observations.

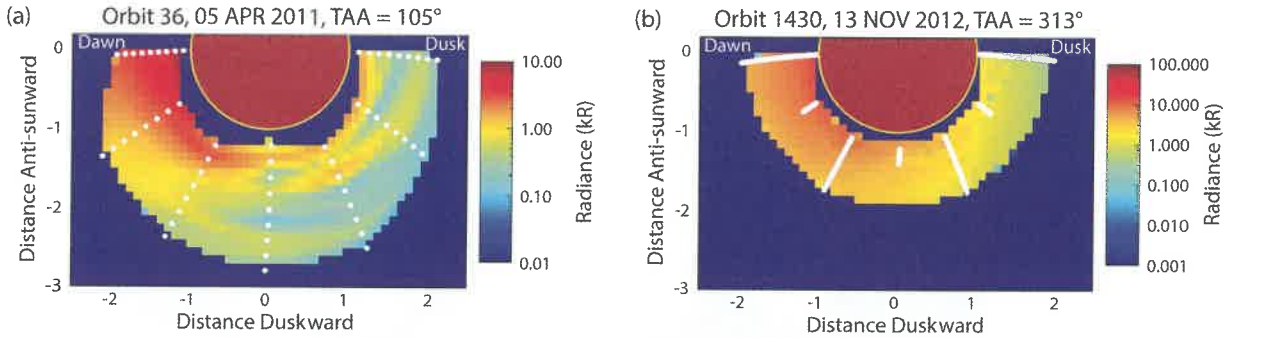

Figure 15.9. Simulated images of Ca emission in Mercury's dayside equatorial plane at two locations in Mercury's orbit were produced by interpolating between observations obtained at the white points approximately perpendicular to the plane of these images (Burger et al., 2014). In each image, dawn is to the left and the Sun is down. The white points represent positions where the UVVS line of sight crosses the equatorial plane; the altitude sampling is higher in the right panel. The images reflect large-scale local-time variations (small-scale variations in the images are not real). Although the magnitude of the emission varies with Mercury true anomaly, Ca is always brightest in the dawn hemisphere, usually, but not always, peaking at dawn.

The robust nature of the year-to-year repeatability and nearly constant near-surface exospheric temperature were unexpected. These findings are surprising in light of the published ground-based observations, which have suggested that sodium is ejected from the surface by a complex mixture of processes. However, because of the geometrical limitations of the UVVS limb scans, with a tangent point almost always at low latitudes on the dayside, a global model is precluded from these data.

15.3.2 Calcium

15.3.2.1 Observations

Prior to MESSENGER, ground-based observations identified Ca mainly over the poles and in the anti-sunward direction (Killen et al., 2005). Significant Ca emission (>2 kR) was seen up to two planetary radii behind the planet. The lines of sight for ground-based observations are limited in their ability to separate source regions in the east–west (i.e., dawn–dusk) direction, and scattering from the surface precluded observations near the dayside. During MESSENGER's Mercury flybys, UVVS observations were able to isolate dawn from dusk, and it was seen that the source of Ca is highly concentrated in the dawn equatorial region (Figure 15.9) (McClintock et al., 2009; Vervack et al., 2010; Burger et al., 2012).

The temperature was also determined to be extremely high on the basis of the scale height of Ca observed above Mercury's poles and by the fact that Ca extends into the tail region despite the short photoionization lifetime (<1 h) (McClintock et al., 2009). Once MESSENGER was in orbit, UVVS began near daily (i.e., at least one orbit per Earth day) observations of Ca. Although its abundance in the exosphere is small compared with those of Na, H, and Mg, Ca is easily detected by UVVS owing to a combination of calcium's high scattering probability at a wavelength where the solar flux is large and the high sensitivity of the instrument at that wavelength.

The calcium in Mercury's exosphere appears to originate from a region near the dawn equatorial point, but the source may move toward mid-morning at some true anomaly angles. Burger et al. (2012) studied the UVVS Ca data from the MESSENGER flybys of Mercury and the first seven orbits of the orbital science phase of the mission. Burger et al. (2014) extended this study to include dayside limb scans from MESSENGER's primary mission (18 March 2011 to 17 March 2012) and first extended mission (18 March 2012 to 17 March 2013). The Ca observations are well fit by a source centered at dawn that drops off exponentially with an e-folding radius of ~50° of arc. The source appeared to be fixed in local time and was not tied to the surface geology. The models required the atomic Ca source to be extremely energetic: the best fit was found to be ~70,000 K under the assumption that it has a thermal flux distribution (a thermal speed of 5.4 km s^{-1}), or a velocity greater than the escape velocity (4.25 km s^{-1}) if it is characterized by a Gaussian distribution. Burger et al. (2014) found a strong seasonal dependence in the source rate (Figure 15.10), although there was little year-to-year variability. The Ca source rate is greatest at a Mercury true anomaly angle of 20°, shortly after perihelion (TAA = 0°), and reaches a minimum just after aphelion (TAA = 180°).

15.3.2.2 Models

Wurz and Lammer (2003) used a Monte Carlo code that treated thermal release, particle sputtering, photon-stimulated desorption, and micrometeoroid impact to develop Mercury exospheric models for a variety of atomic and molecular species. They assumed that Ca is sputtered from the surface because of the large line width measured by Bida et al. (2000), consistent with a thermal temperature of 12,000 K. Killen et al. (2005) suggested that Ca is vaporized in the form of molecules by micrometeoroid impact and is subsequently dissociated in an exothermic process, releasing additional binding energy.

A Monte Carlo model of Mercury's exosphere was successfully developed to model UVVS observations of Na (Burger et al., 2010; Mouawad et al., 2011) and later was extended to Ca (Burger et al., 2012, 2014). The model follows the evolution of atomic and molecular species ejected from Mercury's surface or produced above the surface by molecular dissociation. Source processes were characterized by the initial spatial and energy distributions of test particles; a fifth-order, variable-step-size Runge–Kutta integrator (Press et al., 2007) was used to solve

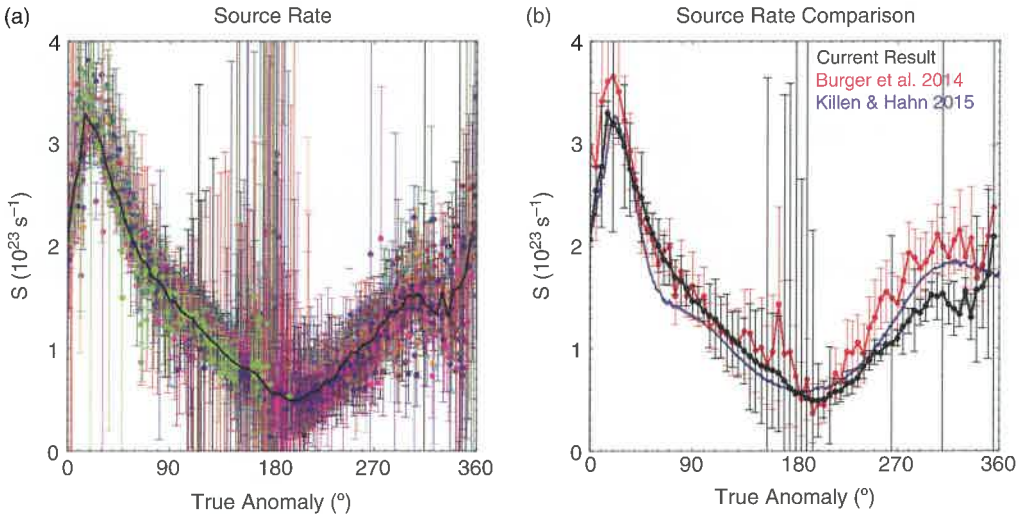

Figure 15.10. (a) Derived source rate S of calcium for a source temperature of 70,000 K and an exponential fall off from the dawn equatorial point with an e-folding distance of 50° of arc along Mercury's surface (Christou et al., 2015). Each point represents a model of a single MESSENGER orbit; 2375 orbits from the first 16 Mercury years of the MESSENGER mission were used. The black line shows the mean source rate in bins of width 5° in true anomaly. (b) Comparison of the mean source rate (black) with that derived by Burger et al. (2014) using only the limb scans from the first nine Mercury years (red) and with the micrometeoroid flux determined by Killen and Hahn (2015) scaled to match the data from Burger et al. (2014) (blue).

the equations of motion for these particles under the forces of gravity from Mercury and radiation acceleration caused by the isotropic scattering of solar photons incident from a single direction. In practice, either a constant-step-size Runge–Kutta integrator or the more computationally intensive, but also more accurate and numerically stable, variable-step-size integrator was used.

Because the g-value (emission probability) depends on the solar flux absorbed by the atom, it is a function of the distance from and radial velocity of the atom relative to the Sun. The Burger et al. (2012, 2014) model determines the g-value at each integration step using the instantaneous radial velocity relative to the Sun as computed by the integrator in order to compute radiation pressure acceleration. The g-values for Ca at 272.2 nm, 422.8 nm, and 456.7 nm were calculated as a function of radial velocity by Killen et al. (2009) (>99% of the radiation acceleration is due to the 422.8 nm line). A linear interpolation between tabulated values was used to calculate the g-value at the heliocentric velocity of the atom. Atomic species were tracked by the integrator until they were lost by photoionization, gravitational escape outside the region of interest (~10 R_M), or sticking to the surface. Charge exchange and electron-impact ionization do not contribute significantly to the loss because of the low plasma densities. Similarly, the only emission mechanism considered was resonant scattering of sunlight. However, the ability to include plasma effects on loss and emission was incorporated in the model. It was assumed that Ca atoms that return to the surface stick with 100% efficiency, although the sticking efficiency and thermal accommodation coefficients are adjustable parameters in the model (Burger et al., 2010; Mouawad et al., 2011).

Burger et al. (2012, 2014) assumed Maxwellian flux distributions as a means of estimating the mean energy of the outward-directed Ca. Burger et al. (2014) also demonstrated that Gaussian flux distributions are consistent with the data when the mean velocity is greater than Mercury's escape velocity. This distribution approximates a dissociation source: dissociating Ca-bearing molecules give the fresh neutral Ca atom an energy boost from the excess energy of the dissociating photon, electron, or ion (e.g., Killen, 2015, 2016).

If atomic Ca is produced from the dissociation of Ca-bearing molecules near the surface, the initial speed distribution will be approximately Gaussian, in the form

$$f_v = e^{-(v-v_p)^2/2\eta^2}, \tag{15.14}$$

where v_p is the most probable speed and η is the width of the distribution.

Electron-stimulated desorption (ESD) has also been suggested as a possible source process for Mercury's exosphere (McLain et al., 2011; Schriver et al., 2011). Burger et al. (2012, 2014) found that ESD is an unlikely Ca source, however, owing to the year-to-year stability of the Ca exosphere compared with the solar-wind interaction with Mercury's magnetosphere and the lack of evidence for precipitating electrons at dawn. Killen (2016) concluded that electron impact dissociation (EID) cannot be responsible for the energization of the Ca due to the small cross section for EID.

The atomic calcium in Mercury's exosphere is quickly ionized by solar UV radiation. Burger et al. (2012, 2014) assumed that the photoionization lifetime varied between 23 min at perihelion and 52 min at aphelion, although there is a large uncertainty in these values, as discussed in Section 15.2.2.2.

Burger et al. (2012, 2014) took a data-fitting approach in their study of Ca observations by MASCS. The goal of these studies was to simulate the observed data from the MESSENGER flybys and orbital phase to determine the spatial and energy

distributions of the escaping Ca. Other authors (e.g., Killen and Hahn, 2015; Christou et al., 2015; Killen, 2015, 2016) considered the physical mechanisms responsible for producing the modeled source distributions, concentrating on impact vaporization. A process-driven procedure can be used to determine the expected distributions that MESSENGER would observe for a given process.

Given that the high latitudes were not well observed by the UVVS instrument, the complete mix of Ca source mechanisms is currently somewhat uncertain. Ion sputtering or electron-stimulated desorption were considered unimportant (Burger et al., 2012, 2014) because the magnetosphere is more variable than the data, and ion precipitation is not expected to peak at dawn (Kallio et al., 2008; Benna et al., 2010). Pfleger et al. (2015) computed three-dimensional exosphere models for sputtering by solar-wind H^+ and He^{++} and concluded that solar-wind-sputtered Ca could provide a minor population with respect to the MESSENGER observations. The average dayside number density of Ca produced by solar-wind sputtering was estimated to be less than 1 cm^{-3}, which would probably not be measured by the UVVS instrument but would not be insignificant relative to the 1–4 cm^{-3} peak Ca density reported by Burger et al. (2014). Pfleger et al. (2015) concluded that a dayside Ca surface density comparable to the long-term observations could be expected from extreme solar events. Unfortunately, the UVVS instrument either went into safe hold or was overwhelmed by noise during extreme solar wind events and could not measure the response of the exosphere to these solar events.

The most promising hypothesis for the production of the Ca exosphere is that the primary source is micrometeoroid impact vaporization, which produces Ca-bearing molecules or ions that quickly dissociate to produce energetic Ca atoms (Killen, 2015). This idea was first proposed by Killen et al. (2005) and was considered by Burger et al. (2014). There are several features that make this proposal attractive. First, recent radar observations and models of micrometeoroids at Earth show that there is a strong dawn enhancement in the impactor flux (Janches et al., 2006; Pifko et al., 2013). Horanyi et al. (2015) reported a dawn–dusk asymmetry in dust at the Moon from LADEE dust observations. They indicated that the dust flux at dawn can be up to a factor of 6 larger than at dusk, in contrast to estimates of a factor of 3 dawn-to-dusk ratio of dust influx at Earth (Pifko et al., 2013).

Calcium-bearing molecules are more likely to be produced in impact vapor plumes than atomic Ca (Berezhnoy and Klumov, 2008), and the molecules expected to be produced (CaO, CaOH, and/or $Ca(OH)_2$, depending on the temperature of the vapor plume) quickly dissociate to release atomic Ca (Berezhnoy and Klumov, 2008; Berezhnoy, 2013). Killen (2015) estimated that the most likely mechanism for creating high-energy atomic Ca is dissociative ionization of precursor molecules. Killen and Hahn (2015) showed that the total Ca source rate is consistent with the dust flux expected as Mercury traverses the interplanetary dust disk and, in addition, intersects a cometary dust stream near true anomaly 25° (Figure 15.11), possibly associated with comet 2P/Encke (Christou et al., 2015). They did not estimate probable dawn–dusk asymmetries.

The exospheric Ca source is unlikely to be adsorbed Ca-bearing material on the nightside that thermally desorbs as it enters sunlight, because the models of Burger et al. (2012) required a pre-dawn Ca source and because the temperature required to vaporize Ca is over 3000 K.

Pfleger et al. (2015) concluded that sputtering could be responsible for an important fraction of the Ca exosphere, slightly below detectability by the UVVS instrument. This finding might explain the Ca observed over Mercury's poles in ground-based spectra (e.g., Killen et al., 2005) and possibly the enhancement of Ca over the poles during the third MESSENGER flyby (Vervack et al., 2010).

15.3.3 Magnesium

The discovery measurements of magnesium (Mg) obtained during MESSENGER's second Mercury flyby were modeled to constrain the source and loss processes for this species (Killen et al., 2010; Sarantos et al., 2011). These measurements provided a unique opportunity for constraining the portion of the exosphere produced by energetic processes, because they probed ejecta at very large downtail distances that could not be probed again after MESSENGER's orbit insertion. The flyby data were matched to Chamberlain models (Killen et al., 2010; Sarantos et al., 2011) and non-uniform sputtering models (Sarantos et al., 2011) in which transport was computed from Liouville's theorem (i.e., gravity forces were included but not radiation pressure or losses to photoionization). Sarantos et al. (2011) found that the distribution of magnesium with tail distance is suggestive of possibly two energetic ejection processes, because the superposition of a hot source ($T_{HOT} \geq 20{,}000$ K) with a cooler source ($T_{COOL} \leq 5000$ K) improved the description of emission detected in the near and far tail (Figure 15.12). The more energetic component populating the tail required higher rates by a factor of at least 5 than ion sputtering could provide under the solar-wind conditions prevailing during the flyby (Sarantos et al., 2011). This conclusion is subject to some uncertainty, however, both from modeling access of the solar wind to the surface and from the fact that the g-value was used for atoms at rest with respect to Mercury.

Dayside limb scans and near-tail measurements during MESSENGER's orbital phase provide evidence for a non-uniform Mg source. Analysis of individual limb scans with Chamberlain fits provides convincing evidence for a dawn–dusk asymmetry with peak dayside abundances at local times of 8–10 h (Merkel et al., 2017). Given only limb scan data, the necessity for two temperature components on the dayside is unclear, as these data can be fit with a single source at 5000 K on most days. The source of exospheric Mg appears to originate near dawn or in the mid-morning (Figure 15.13).

The main conclusion from Sarantos et al. (2011) was that the total amount of magnesium at altitudes exceeding 100 km is consistent with predictions from impact vaporization models if micrometeoroid impacts eject both Mg atoms and Mg-bearing molecules (e.g., MgO, MgS) with molecular dissociation lifetimes of no more than 2 min (Figure 15.14). It is conceivable that reactions taking place during a fireball expansion result in at least half of the magnesium being bound in molecules (Berezhnoy and Klumov, 2008). Longer dissociation lifetimes would require a mix of hot atoms from dissociating molecules and fast atoms from sputtering. Observations taken at low

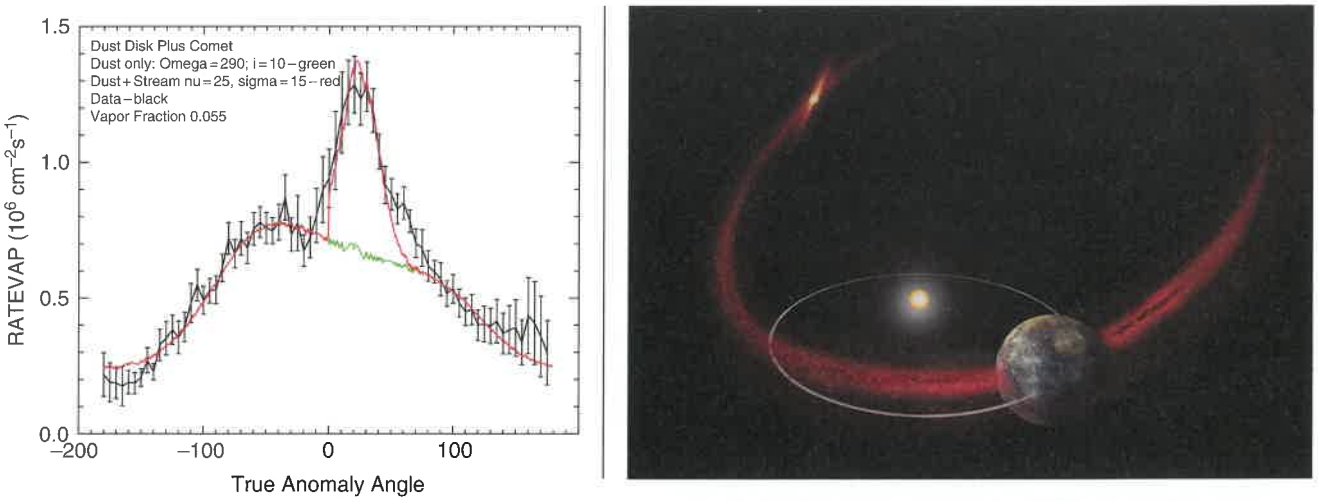

Figure 15.11. (Left) Derived source rate of Ca from the first nine Mercury years of UVVS observations plotted as a function of Mercury true anomaly angle, along with the modeled hot component of impact vaporization by the flux from interplanetary dust disk onto Mercury (green) with the addition of dust from the comet 2P/Encke centered near 25° (red) (Killen and Hahn, 2015). Away from 0–70° TAA the red line follows the dust-disk-only curve. (Right) Artist's conception of comet dust impacting Mercury (not to scale).

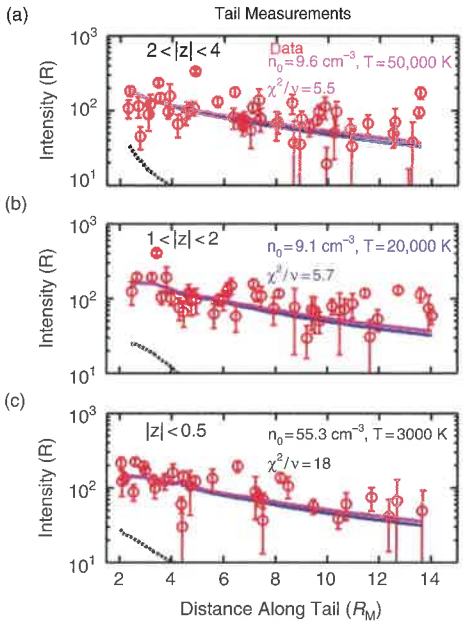

Figure 15.12. Magnesium 285-nm cross-tail line-of-sight radiances (red circles) measured down the tail to 14 Mercury radii (R_M) are compared at vertical distances from the equator of (a) (2–4) R_M (b) (1–2) R_M, and (c) (–0.5–0.5) R_M. Models based on source temperatures 50,000 K (magenta) and 20,000 K (blue) are indistinguishable, and both fit the data. The model prediction for a 3000 K source lies well below the data for all vertical distances. From Sarantos et al. (2011).

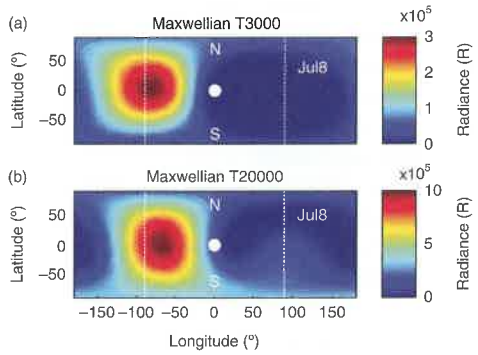

Figure 15.13. The derived Mg flux from the surface (atoms cm^{-2} s^{-1}) on 8 July 2012, under the assumption of a Maxwellian velocity distribution for released ejecta. The data are consistent with a warm component at 3000 K covering the dawn hemisphere and a hot component at about 20,000 K in the morning quadrant. The white dot denotes the subsolar point, and the dawn terminator is at –90° longitude (vertical dotted line to the left). Other fits are possible, including a single source at 5000 K. Adapted from Sarantos et al. (2012).

spacecraft altitudes just nightward of the dawn terminator region and before crossing to the dayside could be interpreted as indicative of thermally accommodated particles (Sarantos et al., 2011). Data from the third MESSENGER flyby, which could provide equally important constraints for hot processes, have not been modeled. Both Mg and Ca exhibit a very hot component, but that for Ca (~70,000 K) (Burger et al., 2014) is more energetic than that for Mg (~20,000 K). However, this temperature was derived under the assumption of a short photoionization lifetime. Both Ca and Mg require some process in addition to impact vaporization to provide the additional energy, and their observed energies are consistent with the dissociation of a precursor molecule (e.g., Killen, 2015) or sputtering. Presumably a sputtered component should be seen at high latitudes (Pfleger et al., 2015), in contrast to the observed distributions peaking at the equator (Sarantos et al., 2012). There is no evidence for a 3000–5000 K component for the Ca exosphere as there is for Mg.

Sarantos et al. (2012) fit limb scans and tail data from the first three Mercury years after MESSENGER's orbit insertion by employing a Monte Carlo model that included the effects of photoionization, radiation pressure, and velocity-dependent

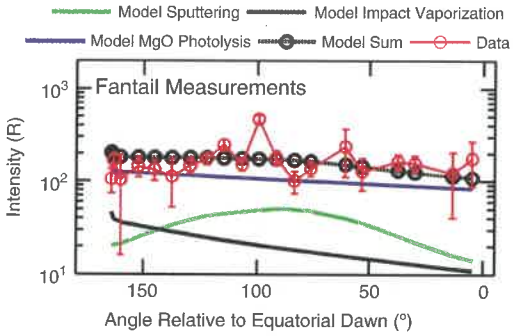

Figure 15.14. Fantail measurements of the Mg emission during the second MESSENGER flyby (McClintock et al., 2009) are best fit with a model of MgO dissociation (Sarantos et al., 2011). The addition of smaller contributions from impact vaporization and sputtering yields a better total fit to the details of the observations (red circles with error bars).

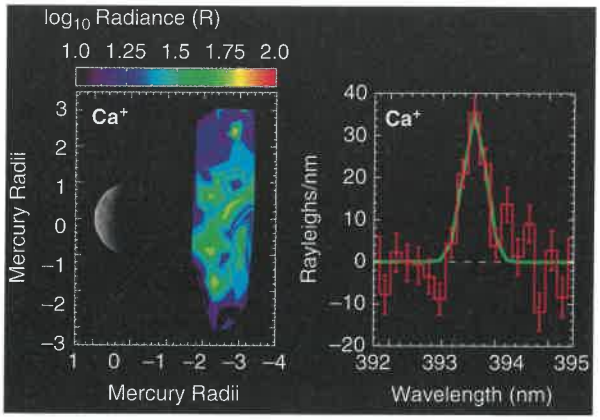

Figure 15.15. (Left) This pseudo-image of the Ca^+ emission detected during the third MESSENGER flyby was generated by projecting the observed column emissions onto a plane containing the Sun–Mercury line and the planet's spin axis and interpolating to fill in unobserved regions. (Right) The red spectrum represents the average of all the Ca^+ emission-line observations (one-standard-deviation error bars are shown) during the third flyby; the green line is a Gaussian fit to the average Ca^+ line. Adapted from Vervack et al. (2010).

g-values. They used combinations of ejection processes with Maxwellian and sputtered initial distributions. The three-dimensional output from each tested source process was discretized in a way that enabled searches for non-uniform ejection in a systematic manner. A Monte Carlo method was used to eject test particles within each of 2000 surface patches for each assumed source temperature. These particles, which were traced until photoionization or contact with the surface, represent the mapping of a "unit flux" moving from one surface element into the three-dimensional (3D) volume. Output from the modeled surface elements was saved separately, and a linear combination of the modeled intensities from each was fit to the emission data using a penalized least-squares regression method. The retrieved unknown variables are the fluxes leaving each surface patch. Such a method was used to estimate the best spatial release pattern that fit the data each day under the assumption of a given velocity distribution function for released ejecta.

15.3.4 Ionized Calcium

Ionized calcium (Ca^+) was observed close to the equatorial plane in a relatively small region approximately (1–2) R_M tailward of the planet on the third MESSENGER flyby (Vervack et al., 2010), as shown in Figure 15.15. Similar line-of-sight column densities for Ca^+ and Ca were measured, an unlikely phenomenon if Ca^+ is produced locally by ionization of Ca because of large differences in their respective observed velocities (Ca, several km s^{-1}; Ca^+ up to hundreds of km s^{-1}). The observations occurred tailward of the magnetospheric X-line while the spacecraft was inbound and lend support for the view that a magnetospheric convection pattern led to a concentration of Ca^+ in the region behind the X-line before the Ca^+ ions were ejected down the tail. UVVS intensities compared favorably with those reported by Bida and Killen (2017) from observations at the Keck 1 telescope of a region (1.7–2.0) R_M from planet center (Section 14.4.5.5). This observation corresponds to about a factor of 5 greater than the three-standard-deviation abundance measured on 15 May 2008 and 3 May 2009 (Bida and Killen, 2011, 2017). Bida and Killen (2017) obtained an upper limit to the Ca^+ column equal to 3.9×10^6 cm^{-2} at approximately the same altitude (1630 km above the limb) as the UVVS observation.

The lifetime of Ca against photoionization is short, ~1500 s (Huebner and Mukherjee, 2015), so most exospheric Ca^+ ions are formed within 2.5 R_M and the Ca^+ pickup process occurs within Mercury's magnetosphere. The Ca^+ produced over a relatively large volume might be concentrated by magnetospheric convection into the near-tail equatorial region. Vervack et al. (2010) estimated that although Ca^+ would fill the entire width of the magnetotail, only about 65% of the Ca^+ was in sunlight where it would have been observable by the UVVS.

15.3.5 Weakly Emitting or Less Abundant Species

Although it was expected that emission from several weaker or less abundant species such as Al, Fe, and Ca^+ would be detected with some regularity in Mercury's exosphere, such an expectation was not met. The MESSENGER UVVS observations in particular are interesting in that no emission from Al, Ca^+, or Mn was detected during the orbital phase until late in the mission (the final Earth year in orbit) (Vervack et al., 2011, 2015, 2016). These species have been elusive both from the ground and from MESSENGER observations, pointing to a high level of variability. Even more interesting is that all of the detections of these species have been confined to a particular spatial and temporal pattern. Spatially, all the detections of these three species by UVVS during the orbital phase of MESSENGER occurred in the pre-dawn nightside region (local times around 2–5 h). Also, they were detected only during the outbound leg of Mercury's orbit, between true anomaly angles of 0° and 70° (Vervack et al., 2016). Aluminum was detected from ground-based observations with the Keck I telescope at TAA 103° and 117°, farther from perihelion but still on the outbound leg of the orbit (Bida and Killen, 2017).

The location and timing of these detections is highly suggestive of a connection to the comet 2P/Encke dust stream that was proposed by Killen and Hahn (2015) to explain the spike in the Ca emission over similar true anomaly angles (see Section 15.3.2.2). Dust from Encke impacting the dawn side of the planet may have led to an enhancement in these species to levels that were detectable by UVVS. It is also possible that some of the material may be cometary in origin. The marked difference in the observed profile for Mn (Figure 14.45) compared with those for Al and Ca^+ may indicate that Mn perhaps derives from the cometary dust rather than the surface of Mercury itself.

The Encke stream may also explain why these species were not detected by UVVS earlier in the mission, despite observations at the same general location and time. Due to the ecccentricity of Mercury's orbit, Mercury's terminator moves backward (toward the nightside) from a TAA of about 340° to TAA 20°. A delayed source as a result of this rock-back of the terminator pre-perihelion would exhibit the same source rate every Mercury year, counter to the observations. Comet streams at Earth are responsible for meteor showers, and occasionally there are larger "clumps" of dust that lead to more spectacular meteor storms. Such behavior is not uncommon with the Taurids at Earth, which also derive from comet Encke (Jenniskens, 2006). A similar change in the amount of dust that is impacting Mercury in a given year (or years) could account for the onset of detection of these species by UVVS. Furthermore, it may not be coincidental that Encke had a very close passage to Mercury in 2013, and these detections began three Mercury years later.

15.4 CONCLUSIONS AND UNANSWERED QUESTIONS

Observations of exospheric Ca and Mg show that their respective exospheres are very hot, much hotter than can be explained by impact vaporization. Although sputtering can certainly produce vapor that is as hot as that measured for these species, Mercury's magnetosphere generally shields the surface from direct penetration by solar wind except at the cusps (Raines et al., 2013). It is unlikely, on the grounds of both measured sputtering yields and inferred ion fluxes to the surface, that the Ca and Mg exospheres are wholly produced by a sputter source. Killen et al. (2005) suggested that the hot vapor could be produced by dissociation of a molecular precursor. Subsequently Berezhnoy (2013) calculated the equilibrium fraction of various atomic and molecular species produced by impact vaporization and concluded that CaO or $Ca(OH)_2$ would be the most likely calcium-bearing species in the fireball at the quenching temperatures of greater or less than ~3750 K, respectively. Killen (2015) looked at the likely energy of various dissociation mechanisms and concluded that dissociative ionization would be the most likely candidate to produce escaping Ca. There has been no work on the production of hot Mg, which appears to have either a mixture of 3000 K and 20,000 K components, or a single 5000 K component (Sarantos et al., 2012; Merkel et al., 2017). Further analysis of the UVVS Mg observations is required to determine the true energy distribution for Mg and the likely source processes. Further work is also needed to determine the effect of high-mass and high-energy ions that may penetrate to the surface more widely.

The enhanced abundance of Ca seen following perihelion, at a TAA of about 25°–30°, has been attributed to enhanced impact vaporization by a meteoroid shower due to comet 2P/Encke, which is known to cross Mercury's orbit (Killen and Hahn, 2015; Christou et al., 2015). Observations of other species, such as Al, Mn, and Ca^+, may also be enhanced by this cometary dust stream's impact on Mercury. The primarily dawnward location of the Mg source suggests that hot Mg atoms could be produced by the same physical process as the hot Ca. In order for micrometeoroid impacts to be responsible for producing gaseous Mg and Ca around Mercury, models of micrometeoroid precipitation onto Mercury's surface must account for the production of molecules with a dawn–dusk asymmetry. It is likely that the Mg and Ca sources centered near dawn are correlated with impacting dust peaking in Mercury's ram direction, as seen at the Moon (Szalay and Horanyi, 2016). Because the ram direction moves with TAA (Figure 15.16), the dawn sources may shift to slightly pre- or post-dawn locations over the course of a Mercury year. The combined source fluxes of Mg and Ca inferred from orbital phase data locally approach 2×10^6 atoms cm^{-2} s^{-1}, consistent with the flyby results, and may be provided by impacts as previously surmised.

Despite targeting observations at wavelengths near the oxygen 130.4 nm triplet for over 16 Mercury years, no detection was found in the UVVS observations. However, the analysis is difficult owing to scattered solar O emission from the dayside. If the impact vapor produces oxides rather than atomic oxygen and if the oxide is dissociated, an extremely hot O corona would be produced. A very tenuous oxygen corona would by its nature be difficult to observe. However, MESSENGER's Fast Imaging Plasma Spectrometer observed a group of ions, including possible constituents O, OH, and H_2O. If a mass spectrometer with higher mass resolution were flown on a future mission, then it would be possible to separate these components and to determine the true oxygen abundance at the spacecraft altitude.

UVVS observations of sodium did not uncover conclusive evidence for a sputtered component, in contrast to expectations from ground-based observations (e.g., Potter et al., 2006; Mangano et al., 2015; Pfleger et al., 2015). One possible explanation is that most of the data over the dayside, and almost all of the data that were analyzed by Cassidy et al. (2015), were taken at low latitudes. UVVS limb scans were most often taken tangent to the equatorial limb while looking from south to north; thus, they would have missed a high-latitude source near the cusp region for the most part. Future observations that fill this gap in coverage would be worthwhile.

High northern latitudes should be targeted in the future to determine whether meteoroid showers expected to result from comets Bradfield (at TAA 130°) and Tempel–Tuttle lead to enhancements in the region of impact. Concurrent measurement of the dust flux onto Mercury, and especially its spatial distribution with respect to leading and trailing hemispheres and expected meteoroid streams, is highly desirable.

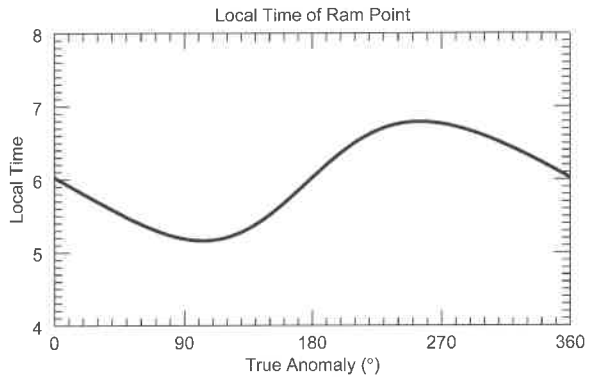

Figure 15.16. The ram point (local time of the orbital velocity vector) moves as a function of true anomaly angle because of the non-uniform relationship between orbital velocity and rotational velocity as a result of Mercury's eccentric orbit.

Mercury's surface composition is highly non-uniform (Weider et al., 2015). A correlation has been found between the local surface composition and the Mg exosphere (Merkel et al., 2018). Further investigations should seek correlations between the exosphere and underlying surface, especially between regions for which there is a large difference in composition.

Although there have been ground-based detections of potassium in Mercury's exosphere from observations of the strong 766.3 nm D_2 line, this wavelength was outside the range of UVVS. Searches for K with UVVS had to use the weaker lines at 404.5 and 404.8 nm (with a combined g-value of <0.07). To date, no K has been detected by UVVS. The Na/K ratio in Mercury's exosphere has been reported to be quite high, but this result may be due to a difference in the spatial distribution of the two species. Doressoundiram et al. (2010) reported Na/K in Mercury's exosphere to be between 80 and 400. Killen et al. (2010) reported Na/K between 22 and 49 at times when the signal-to-noise ratio of the K observation was >5. The large variations in the measured ratios are not surprising in light of the large variation in the surficial K abundance, reported by Peplowski et al. (2012) to be between 300 and 2400 ppm, whereas the Na wt% varies by only about a factor of ~2 from 2.6 wt% in the equatorial regions to 5 wt% at high northern latitudes (Peplowski et al., 2014).

A factor of approximately 2.3 was found between the surface Na/Si weight ratios in the northern polar and equatorial regions, respectively, from MESSENGER Gamma-Ray Spectrometer (GRS) data (Peplowski et al., 2014). Peplowski et al. sought to determine whether the sodium could have been redistributed through desorption in equatorial regions and redeposition and cold trapping near the poles. If redistribution is not an important process, then the composition of the polar regions may represent the original Na abundance in that region. Invoking the assumption that the Na content is lowest in regions that experience maximum near-surface temperatures above 400 K and from temperature maps at the surface and at a depth of 7 cm (Vasavada et al., 1999), Peplowski et al. (2014) concluded that the measured Na distribution supports the hypothesis that the equatorial Na abundances are consistent with depletion via thermal modification similar to that proposed for K by Peplowski et al. (2012), who found a correlation between the distribution of measured surficial K abundances and models of the maximum temperature. Cassidy et al. (2016), on the other hand, found a correlation between Na abundance in the dawn exosphere and the equatorial temperature at Mercury's hot and cold poles. Other species, notably Mg and Ca, have highly heterogeneous distributions of surface composition (Weider et al., 2015).

REFERENCES

Benna, M., Anderson, B. J., Baker, D. N., Boardsen, S. A., Gloeckler, G., Gold, R. E., Ho, G. C., Killen, R. M., Korth, H., Krimigis, S. M., Purucker, M. E., McNutt, R. L., Raines, J. M., McClintock, W. E., Sarantos, M., Slavin, J. A., Solomon, S. C. and Zurbuchen, T. H. (2010). Modeling of the magnetosphere of Mercury at the time of the first MESSENGER flyby, *Icarus*, **209**, 3–10, doi:10.1016/j.icarus.2009.11.036.

Berezhnoy, A. A. (2013). Chemistry of impact events on the Moon. *Icarus*, **226**, 205–211, doi:10.1016/j.icarus.2013.05.030.

Berezhnoy, A. A. and Klumov, B. A. (2008). Impacts as sources of the exosphere on Mercury. *Icarus*, **195**, 511–522, doi:10.1016/j.icarus.2008.01.005.

Bida, T. A. and Killen, R. M. (2011). Observations of Al, Fe and Ca^+ in Mercury's exosphere. *EPSC-DPS Joint Meeting Abstracts and Program*, **6**, EPSC-DPS2011-1621. European Planetary Science Congress–Division for Planetary Sciences Joint Meeting, Nantes, France, October 2–7.

Bida, T. A. and Killen, R. M. (2017). Observations of the minor species Al and Fe in Mercury's exosphere. *Icarus*, **289**, 227–238, doi:10.1016/j.icarus.2016.10.019.

Bida, T. A., Killen, R. M. and Morgan, T. H. (2000). Discovery of calcium in Mercury's atmosphere. *Nature*, **404**, 159–161.

Borin, P., Bruno, M., Cremonese, G. and Marzari, F. (2010). Estimate of the neutral atoms' contribution to the Mercury exosphere caused by a new flux of micrometeoroids. *Astron. Astrophys.*, **517**, A89, doi:10.1051/0004-6361/201014312.

Burger, M. H., Killen, R. M., Vervack, R. J., Jr., Bradley, E. T., McClintock, W. E., Sarantos, M., Benna, M. and Mouawad, N. (2010). Monte Carlo modeling of sodium in Mercury's exosphere during the first two MESSENGER flybys. *Icarus*, **209**, 63–74.

Burger, M. H., Killen, R. M., McClintock, W. E., Vervack, R. J., Jr., Merkel, A. W., Sprague, A. L. and Sarantos, M. (2012). Modeling MESSENGER observations of calcium in Mercury's exosphere. *J. Geophys. Res.*, **117**, E0L11B, doi:10.1029/2012JE004158.

Burger, M. H., Killen, R. M., McClintock, W. E., Merkel, A. W., Vervack, R. J., Jr., Cassidy, T. A. and Sarantos, M. (2014). Seasonal variations in Mercury's dayside calcium exosphere. *Icarus*, **238**, 51–58, doi:10.1016/j.icarus.2014.04.049.

Cassidy, T. A. and Johnson, R. E. (2005). Monte Carlo model of sputtering and other ejection processes within a regolith. *Icarus*, **176**, 499–507.

Cassidy, T. A., Merkel, A. W., Burger, M. H., Sarantos, M., Killen, R. M., McClintock, W. E. and Vervack, R. J., Jr. (2015). Mercury's seasonal sodium exosphere: MESSENGER orbital observations. *Icarus*, **248**, 547–559, doi:10.1016/j.icarus.2014.10.037.

Cassidy, T. A., McClintock, W. E., Killen, R. M., Sarantos, M., Merkel, A. W., Vervack, R. J., Jr. and Burger, M. H. (2016). A cold-pole enhancement in Mercury's sodium exosphere. *Geophys. Res. Lett.*, **43**, 11,121–11,128.

Christou, A. A., Killen, R. M. and Burger, M. H. (2015). The meteoroid stream of comet Encke at Mercury: Implications for MErcury Surface, Space ENvironment, GEochemistry, and Ranging observations of the exosphere. *Geophys. Res. Lett.*, **42**, 7311–7318, doi:10.1002/2015GL065361.

Cintala, M. J. (1992). Impact-induced thermal effects in the lunar and Mercurian regoliths. *J. Geophys. Res.*, **97**, 947–973.

Combi, M. R., DiSanti, M. A. and Fink, U. (1997). The spatial distribution of gaseous atomic sodium in the comae of comets: Evidence for direct nucleus and extended plasma sources. *Icarus*, **130**, 336–354, doi:10.1006/icar.1997.5832.

Cremonese, G. and Verani, S. (1997). High resolution observations of the sodium emission from the Moon. *Adv. Space Res.*, **19**, 1561–1569, doi:10.1016/S0273-1177(97)00369-4.

Crider, D. H. and Vondrak, R. R. (2003). Space weathering effects on lunar cold trap deposits. *J. Geophys. Res.*, **108** (E7), 5079, doi:10.1029/2002JE002030.

Domingue, D. L., Chapman, C. R., Killen, R. M., Zurbuchen, T. H., Gilbert, J. A., Sarantos, M., Benna, M., Slavin, J. A., Schriver, D., Trávníček, P. M., Orlando, T. M., Sprague, A. L., Blewett, D. T., Gillis-Davis, J. J., Feldman, W. C., Lawrence, D. J., Ho, G. C., Ebel, D. S., Nittler, L. R., Vilas, F., Pieters, C. M., Solomon, S. C., Johnson, C. L., Winslow, R. M., Helbert, J., Peplowski, P. N., Weider, S. Z., Mouawad, N., Izenberg, N. R. and McClintock, W. E. (2014). Mercury's weather-beaten surface: Understanding Mercury in the context of lunar and asteroidal space weathering studies. *Space Sci. Rev.*, **181**, 121–214, doi:10.1007/s11214-014-0039-5.

Doressoundiram, A., Leblanc, F., Foellmi, C., Gicquel, A., Cremonese, G., Donati, J.-F. and Veillet, C. (2010). Spatial variations of the sodium/potassium ratio in Mercury's exosphere uncovered by high-resolution spectroscopy. *Icarus*, **207**, 1–8, doi:10.1016/j.icarus.2009.11.020.

Dzioba, S. and Kelly, R. (1980). On the kinetic energies of sputtered excited particles II. Theory and applications to group IIA fluorides. *Surf. Sci.*, **100**, 119–134.

Farrell, W. M., Hurley, D. M. and Zimmerman, M. I. (2015). Solar wind implantation into lunar regolith: Hydrogen retention in a surface with defects. *Icarus*, **255**, 116–126, doi:10.1016/j.icarus.2014.09.014.

Farrell, W. M., Stubbs, T. J., Vondrak, R. R., Delory, G. T. and Halekas, J. S. (2007). Complex electric fields near the lunar terminator: The near-surface wake and accelerated dust. *Geophys. Res. Lett.*, **34**, L14201, doi:10.1029/2007GL029312.

Gerasimov, M. V., Dikov, Yu. P., Yakolev, O. I., Wlotzka, F. and Distler, V. V. (1999). The volatility of microelements during impact vaporization of meteorites. *Meteorit. Planet. Sci.*, **34**, Suppl., A42.

Hofer, W. O. (1991). Angular, energy, and mass distribution of sputtered particles. In *Sputtering by Particle Bombardment III*, ed. R. Behrisch and K. Wittmaack, Topics in Applied Physics, Vol. 64. Berlin: Springer-Verlag, pp. 15–90.

Holmlid, L. (2006). The alkali metal atmospheres on the Moon and Mercury: Explaining the stable exospheres by heavy Rydberg matter clusters. *Planet. Space Sci.*, **54**, 101–112, doi:10.1016/j.pss.2005.10.005.

Horanyi, M., Szalay, J. R., Kempf, S., Schmidt, J., Grun, E., Srama, R. and Sternovsky, Z. (2015). A permanent, asymmetric dust cloud around the Moon. *Nature*, **522**, 324–326, doi:10.1038/nature14479.

Horanyi, M., Szalay, J. R., Grun, E., Glenar, D., Wang, X. and Zakharov, A. (2016). The dust environment of the Moon. *New Views of the Moon*, abstract 6005. Houston, TX: Lunar and Planetary Institute.

Hornung, K., Malama, Y. G. and Kestenboim, K. S. (2000). Impact vaporization and ionization of cosmic dust particles. *Astrophys. Space Sci.*, **274**, 355–363.

Huebner, W. F. and Mukherjee, J. (2015). Photoionization and photodissociation rates in solar and blackbody radiation fields. *Planet. Space Sci.*, **106**, 11–45, doi:10.1016/j.pss.2014.11.022.

Huebner, W. F., Keady, J. J. and Lyon, S. P. (1992). Solar photo rates for planetary atmospheres and atmospheric pollutants. *Astrophys. Space Sci.*, **195**, 1–294.

Hunten, D. M. and Sprague, A. L. (1997). Origin and character of the lunar and mercurian atmospheres. *Adv. Space Res.*, **19**, 1551–1560, doi:10.1111/j.1945-5100.2002.tb00888.x.

Hunten, D. M. and Sprague, A. L. (2002). Diurnal variation of sodium and potassium at Mercury. *Meteorit. Planet. Sci.*, **37**, 1191–1195, doi:10.1111/j.1945-5100.2002.tb00888.x.

Hunten, D. M., Morgan, T. H. and Shemansky, D. E. (1988). The Mercury atmosphere. In *Mercury*, ed. F. Vilas, C. R. Chapman and M. S. Matthews. Tucson, AZ: University of Arizona Press, pp. 562–612.

Ip, W.-H. (1986). The sodium exosphere and magnetosphere of Mercury. *Geophys. Res. Lett.*, **13**, 423–426.

Janches, D., Heinselman, C. J., Chau, J. L., Chandran, A. and Woodman, R. (2006). Modeling the global micrometeor input function in the upper atmosphere observed by high power and large aperture radars. *J. Geophys. Res.*, **111**, A07317, doi:10.1029/2006JA011628.

Jenniskens, P. (2006). *Meteor Showers and Their Parent Comets*. Cambridge: Cambridge University Press, 752 pp.

Johnson, R. E. (1990). *Energetic Charged-Particle Interactions with Atmospheres and Surfaces*. Berlin: Springer.

Johnson, R. E., Leblanc, F., Yakshinskiy, B. V. and Madey, T. E. (2002). Energy distributions for desorption of sodium and potassium from ice: The Na/K ratio at Europa. *Icarus*, **156**, 136–142.

Jurac, S., Baragiola, R. A., Johnson, R. E. and Sittler, E. C. (1995). Charging of ice grains by low-energy plasmas: Application to Saturn's E-ring. *J. Geophys. Res.*, **100**, 14,821–14,831.

Kallio, E, Wurz, P., Killen, R. M., McKenna-Lawlor, S., Milillo, A., Mura, A., Massetti, S., Orsini, S., Lammer, H., Janhunen, P. and Ip, W.-H. (2008). On the impact of multiply charged heavy solar wind ions on the surface of Mercury, the Moon and Ceres. *Planet. Space Sci.*, **56**, 1506–1516.

Keller, L. P. and McKay, D. S. (1997). The nature and origin of rims on lunar soil grains. *Geochim. Cosmochim. Acta*, **61**, 2331–2341, doi:10.1016/S0016-7037(97)00085-9.

Killen, R. M. (2015). Processes producing the extremely hot Ca and Mg exospheres at Mercury. Presented at 2015 Fall Meeting, American Geophysical Union, abstract P53A–2090, San Francisco, CA, 14–18 December.

Killen, R. M. (2016). Pathways for energization of Ca and Mg in Mercury's exosphere. *Icarus*, **268**, 32–36, doi:10.1016/j.icarus.2015.12.035.

Killen, R. M. and Hahn, J. M. (2015). Impact vaporization as a possible source of Mercury's calcium exosphere. *Icarus*, **250**, 230–237, doi:10.1016/j.icarus.2014.11.035.

Killen, R. M., Sarantos, M., Potter, A. E. and Reiff, P. (2004). Source rates and ion recycling rates for Na and K in Mercury's atmosphere. *Icarus*, **171**, 1–19.

Killen, R. M., Bida, T. A. and Morgan, T. H. (2005). The calcium exosphere of Mercury, *Icarus*, **173**, 300–311.

Killen, R. M., Cremonese, G., Lammer, H., Orsini, S., Potter, A. E., Sprague, A. L., Wurz, P., Khodachenko, M. L., Lichtenegger, H. I. M., Milillo, A. and Mura, A. (2007).

Processes that promote and deplete the exosphere of Mercury. *Space Sci. Rev.*, **132**, 433–509, doi:10.1007/s11214-007-9232-0.

Killen, R. M., Shemansky, D. E. and Mouawad, N. (2009). Expected emission from Mercury's exospheric species, and their UV-visible signatures. *Astrophys. J. Suppl. Ser.*, **181**, 351–359.

Killen, R. M., Potter, A. E., Vervack, R. J., Jr., Bradley, E. T., McClintock, W. E., Anderson, C. M. and Burger, M. H. (2010). Observations of metallic species in Mercury's exosphere. *Icarus*, **209**, 75–87, doi:10.1016/j.icarus.2010.02.018.

Killen, R. M., Burger, M. H., Hurley, D. M., Sarantos, M. and Farrell, W. M. (2014). Exospheres from asteroids to planets. In *Asteroids, Comets, Meteors: Book of Abstracts, Helsinki, Finland, 2014*. Helsinki: University of Helsinki, p. 285.

Kurosawa, K., Sugita, S., Kadono, T., Shigemori, K., Hironaka, Y., Ozaki, N., Shiroshita, A., Cho, Y., Sakaiya, T., Fujioka, S., Tachibana, S., Vinci, T., Kodama, R. and Matsui, T. (2010). Roles of shock-induced ionization due to > 10 km/s impacts on evolution of silicate vapor clouds. *Lunar Planet. Sci.*, **41**, abstract 1785.

Leblanc, F. and Johnson, R. E. (2003). Mercury's sodium exosphere. *Icarus*, **164**, 261–281, doi:10.1016/S0019-1035(03)00147-7.

Leblanc, F. and Johnson, R. E. (2010). Mercury exosphere I. Global circulation model of its sodium component. *Icarus*, **209**, 280–300.

Leblanc, F., Delcourt, D. and Johnson, R. E. (2003). Mercury's sodium exosphere: Magnetospheric ion recycling. *J. Geophys. Res.*, **108** (E12), 5136, doi:10.1029/2003JE002151.

Madey, T. E., Yakshinskiy, B. V. and Ageev, V. N. (1998). Desorption of alkali atoms and ions from oxide surfaces: Relevance to origins of Na and K in atmospheres of Mercury and the Moon. *J. Geophys. Res.*, **103**, 5873–5887.

Madey, T. E., Johnson, R. E. and Orlando, T. M. (2002). Far-out surface science: Radiation-induced surface processes in the Solar System. *Surf. Sci.*, **500**, 838–858.

Mangano, V., Milillo, A., Mura, A., Orsini, S., DeAngelis, E., DiLellis, A. M. and Wurz, P. (2007). The contribution of impulsive meteoritic impact vapourization to the Hermean exosphere. *Planet. Space Sci.*, **55**, 1541–1556.

Mangano, V., Massetti, S., Milillo, A., Plainaki, C., Orsini, S., Rispoli, R. and Leblanc, F. (2015). THEMIS Na exosphere observations of Mercury and their correlation with in-situ magnetic field measurements by MESSENGER. *Planet. Space Sci.*, **115**, 102–109, doi:10.1016/j.pss.2015.04.001.

Marchi, S., Morbidelli, A. and Cremonese, G. (2005). Flux of meteoroid impacts on Mercury. *Astron. Astrophys.*, **431**, 1123–1127.

McClintock, W. E., Vervack, R. J., Jr., Bradley, E. T., Killen, R. M., Mouawad, N., Sprague, A. L., Burger, M. H., Solomon, S. C. and Izenberg, N. R. (2009). Mercury's exosphere during MESSENGER's second flyby: Detection of magnesium and distinct distributions of neutral species. *Science*, **324**, 610–613.

McCord, T. B., Taylor, L. A., Combe, J.-P., Kramer, G., Pieters, C. M., Sunshine, J. M. and Clark, R. N. (2011). Sources and physical processes responsible for OH/H_2O in the lunar soil as revealed by the Moon Mineralogy Mapper (M^3). *J. Geophys. Res.*, **116**, E00G05, doi:10.1029/2010JE003711.

McGrath, M. A., Johnson, R. E. and Lanzerotti, L. J. (1986). Sputtering of sodium on the planet Mercury. *Nature*, **323**, 694–696.

McLain, J. L., Sprague, A. L., Grieves, G. A., Schriver, D., Trávníček, P. M. and Orlando, T. M. (2011). Electron-stimulated desorption of silicates: A potential source for ions in Mercury's space environment. *J. Geophys. Res.*, **116**, E03007, doi:10.1029/2010JE003714.

Merkel, A. W., Cassidy, T. A., Vervack, R. J., Jr., McClintock, W. E., Sarantos, M., Burger, M. H. and Killen, R. M. (2017). Seasonal variations of Mercury's magnesium dayside exosphere from MESSENGER observations. *Icarus*, **281**, 46–54, doi:10.1016/j.icarus.2016.08.032.

Merkel, A. W., Vervack, R. J., Jr., Killen, R. M., Cassidy, T. A., McClintock, W. E., Nittler, L. R. and Burger, M. H. (2018). Evidence connecting Mercury's magnesium exosphere to its magnesium-rich surface terrane. *Geophys. Res. Lett.*, **45**, 6790–6797, doi:10.1029/2018GL078407.

Morgan, T. H., Zook, H. and Potter, A. E. (1988). Impact-driven supply of sodium and potassium to the atmosphere of Mercury. *Icarus*, **75**, 156–170.

Mouawad, N., Burger, M. H., Killen, R. M., Potter, A. E., McClintock, W. E., Vervack, R. J., Bradley, E. T., Benna, M. and Naidu, S. (2011). Constraints on Mercury's Na exosphere: Combined MESSENGER and ground-based data. *Icarus*, **211**, 21–36, doi:10.1016/j.icarus.2010.10.019.

Mura, A. (2012). Loss rates and time scales for sodium at Mercury. *Planet. Space Sci.*, **63–64**, 2–7, doi:10.1016/j.pss.2011.08.012.

Mura, A., Milillo, A., Orsini, S. and Massetti, S. (2007). Numerical and analytical model of Mercury's exosphere: Dependence on surface and external conditions. *Planet. Space Sci.*, **55**, 1569–1583.

Mura, A., Wurz, P., Lichtenegger, H. I. M., Schleicher, H., Lammer, H., Delcourt, D., Milillo, A., Orsini, S., Massetti, S. and Khodachenko, M. L. (2009). The sodium exosphere of Mercury: Comparison between observations during Mercury's transit and model results. *Icarus*, **200**, 1–11, doi:10.1016/j.icarus.2008.11.014

Noble, S. K., Keller, L. P. and Pieters, C. (2005). Evidence of space weathering in regolith breccias I: Lunar regolith breccias. *Meteorit. Planet. Sci.*, **40**, 397–408.

Peplowski, P. N., Lawrence, D. J., Rhodes, E. A., Sprague, A. L., McCoy, T. J., Denevi, B. W., Evans, L. G., Head, J. W., Nittler, L. R., Solomon, S. C., Stockstill-Cahill, K. R. and Weider, S. Z. (2012). Variations in the abundances of potassium and thorium on the surface of Mercury: Results from the MESSENGER Gamma-Ray Spectrometer. *J. Geophys. Res.*, **117**, E00L04, doi:10.1029/2012JE004141.

Peplowski, P. N., Evans, L. G., Stockstill-Cahill, K. R., Lawrence, D. J., Goldsten, J. O., McCoy, T. J., Nittler, L. R., Solomon, S. C., Sprague, A. L., Starr, R. D. and Weider, S. Z. (2014). Enhanced sodium abundance in Mercury's north polar region revealed by the MESSENGER Gamma-Ray Spectrometer. *Icarus*, **228**, 86–95, doi:10.1016/j.icarus.2013.09.007.

Pfleger, M., Lichtenegger, H. I. M., Wurz, P., Lammer, H., Kallio, E., Alho, M.., Mura, A., McKenna-Lawler, S. and Martin-Fernandez, J. A. (2015). 3D-modeling of Mercury's solar wind sputtered surface-exosphere environment. *Planet. Space Sci.*, **115**, 90–101, doi:10.1016/j.pss.2015.04.016.

Pifko, S., Janches, D., Close, S., Sparks, J., Nakamura, T. and Nesvorny, D. (2013). The Meteoroid Input Function and predictions of mid-latitude meteor observations by the MU radar. *Icarus*, **223**, 444–459, doi:10.1016/j.icarus.2012.12.014.

Poston, M. J., Grieves, G. A., Aleksandrov, A. B., Hibbitts, C. A., Dyar, M. D. and Orlando, T. M. (2015). Temperature programmed desorption studies of water interactions with Apollo

lunar samples 12001 and 72501. *Icarus*, **255**, 24–29, doi:10.1016/j.icarus.2014.09.049

Potter, A. E. (1995). Chemical sputtering could produce sodium vapor and ice on Mercury. *Geophys. Res. Lett.*, **22**, 3289–3292.

Potter, A. E., Killen, R. M. and Morgan, T. H. (2002). The sodium tail of Mercury. *Meteorit. Planet. Sci.*, 37, 1165–1172.

Potter, A. E., Killen, R. M. and Sarantos, M. (2006). Spatial distribution of sodium on Mercury. *Icarus*, **181**, 1–12, doi:10.1016/j.icarus.2005.10.026.

Potter, A. E., Killen, R. M. and Morgan, T. H. (2007). Solar radiation acceleration effects on Mercury's sodium emission. *Icarus*, **186**, 571–580, doi:10.1016/j.icarus.2006.09.025.

Press, W. H., Teukolsky, S. A., Vetterling, W. T. and Flannery, B. P. (2007). *Numerical Recipes: The Art of Scientific Computing*, 3rd edn. Cambridge: Cambridge University Press.

Raines, J. M., Gershman, D. J., Zurbuchen, T. H., Sarantos, M., Slavin, J. A., Gilbert, J. A., Korth, H., Anderson, B. J., Gloeckler, G., Krimigis, S. M., McNutt, R. L., Jr. and Solomon, S. C. (2013). Distribution and compositional variations of plasma ions in Mercury's space environment: The first three Mercury years of MESSENGER observations. *J. Geophys. Res. Space Physics*, **118**, 1604–1619, doi:10.1029/2012JA018073.

Roth, J. (1983). Chemical sputtering. In *Sputtering by Particle Bombardment II*, ed. R. Behrish, Topics in Applied Physics, Vol. 52. Berlin: Springer-Verlag, pp. 91–146, doi:10.1007/3-540-12593-0_3.

Sarantos, M., Killen, R. M., McClintock, W. E., Bradley, E. T., Vervack, R. J., Jr., Benna, M. and Slavin, J. A. (2011). Limits to Mercury's magnesium exosphere from MESSENGER second flyby observations. *Planet. Space Sci.*, **59**, 1992–2003, doi:10.1016/j.pss.2011.05.002.

Sarantos, M., Killen, R. M., McClintock, W. E., Vervack, R. J., Jr., Merkel, A. W., Burger, M. H., Cassidy, T. A., Slavin, J. A., Sprague, A. L. and Solomon, S. C. (2012). Mercury's Mg exosphere from MESSENGER data. *EPSC Abstracts*, **7**, abstract EPSC2012-707-1. European Planetary Science Congress, Madrid, Spain, 23–28 September.

Schmidt, C. A., Baumgardner, J., Mendillo, M. and Wilson, J. K. (2012). Escape rates and variability constraints for high-energy sodium sources at Mercury. *J. Geophys. Res.*, **117**, A03301, doi:10.1029/2011JA017217.

Schriver, D., Trávníček, P., Ashour-Abdalla, M., Richard, R. L., Hellinger, P., Slavin, J. A., Anderson, B. J., Baker, D. N., Benna, M., Boardsen, S. A., Gold, R. E., Ho, G. C., Korth, H., Krimigis, S. M., McClintock, W. E., McLain, J. L., Orlando, T. M., Sarantos, M., Sprague, A. L. and Starr, R. D. (2011). Electron transport and precipitation at Mercury during the MESSENGER flybys: Implications for electron-stimulated desorption. *Planet. Space Sci.*, **59**, 2026–2036, doi:10.1016/j.pss.2011.03.008.

Schultz, P. (1996). Effect of impact angle on vaporization. *J. Geophys. Res.*, **101**, 21,117–21,136, doi:10.1029/96JE02266.

Sieveka, E. M. and Johnson, R. E. (1984). Ejection of atoms and molecules from Io by plasma-ion impact. *Astrophys. J.*, **287**, 418–426, doi:10.1086/162701.

Sigmund, P. (1969). Theory of sputtering I: Sputtering yields of amorphous and polycrystalline targets. *Phys. Rev.*, **184**, 383–416.

Smith, R. S. and Kay, B. D. (1997). Adsorption, desorption, and crystallization kinetics in nanoscale water films. *Recent Res. Dev. Phys. Chem.*, **1**, 209–219.

Smyth, W. H. (1983). Io's sodium cloud: Explanation of the east–west asymmetries. II. *Astrophys. J.*, **264**, 708–725.

Smyth, W. H. and Marconi, M. L. (1995a). Theoretical overview and modeling of the sodium and potassium atmospheres of the Moon. *Astrophys. J.*, **443**, 371–392.

Smyth, W. H. and Marconi, M. L. (1995b). Theoretical overview and modeling of the sodium and potassium atmospheres of Mercury. *Astrophys. J.*, **441**, 839–864.

Sneh, O., Cameron, M. A. and George, S. M. (1996). Adsorption and desorption kinetics of H_2O on a fully hydroxylated SiO_2 surface. *Surf. Sci.*, **364**, 61–78.

Starukhina, L. V. and Shkuratov, Y. G. (2000). The lunar poles: Water ice or chemically trapped hydrogen?, *Icarus*, **147**, 585–587, doi:10.1006/icar.2000.6476.

Szalay, J. R. and Horanyi, M. (2016). Annual variation and synodic modulation of the sporadic meteoroid flux to the Moon. *Geophys Res. Lett.*, 42, 10,580–10.584, doi:10.1002/2015GL066908.

Vasavada, A. R., Paige, D. A. and Wood, S. E. (1999). Near-surface temperatures on Mercury and the Moon and the stability of polar ice deposits. *Icarus*, **141**, 179–193, doi:10.1006/icar.1999.6175.

Verner, D. A. and Yakovlev, D. G. (1995). Analytic FITS for partial photoionization cross sections. *Astron. Astrophys. Suppl. Ser.*, **109**, 125–135.

Verner, D. A., Yakovlev, D. G., Band, I. M. and Trzhaskovskaya, M. B. (1993). Subshell photoionization cross sections and ionization energies of atoms and ions from He to Zn. *Atom. Data Nucl. Data Tables*, **55**, 233–280.

Verner, D. A., Ferland, G. J., Korista, K. T. and Yakovlev, D. G. (1996). Atomic data for astrophysics. II. New analytic FITS for photoionization cross sections of atoms and ions. *Astrophys. J.*, **465**, 487–498.

Vervack, R. J., Jr., McClintock, W. E., Killen, R. M., Sprague, A. L., Anderson, B. J., Burger, M. H., Bradley, E. T., Mouawad, N., Solomon, S. C. and Izenberg, N. R. (2010). Mercury's complex exosphere: Results from MESSENGER's third flyby. *Science*, **329**, 672–675.

Vervack, R. J., Jr., Killen, R. M., Sprague, A. L., Burger, M. H., Merkel, A. W. and Sarantos, M. (2011). Early MESSENGER results for less abundant or weakly emitting species in Mercury's exosphere. *EPSC-DPS Joint Meeting Abstracts and Program*, **6**, abstract EPSC-DPS2011-1131. European Planetary Science Congress–Division for Planetary Sciences Joint Meeting, Nantes, France, 2–7 October.

Vervack, R. J., Jr., McClintock, W. E., Killen, R. M., Merkel, A. W., Burger, M. H., Sarantos, M. and Cassidy, T. A. (2015). Mercury's exosphere: New detections, discoveries, and insights. *Abstracts, 47th Division for Planetary Sciences Annual Meeting*, abstract 107.01. National Harbor, MD, 8–13 November, pp. 19–20.

Vervack, R. J., Jr., Killen, R. M., McClintock, W. E., Merkel, A. W., Burger, M. H., Cassidy, T. A. and Sarantos, M. (2016). New discoveries from MESSENGER and insights into Mercury's exosphere. *Geophys. Res. Lett.*, **43**, 11,545–11,551.

Weider, S. Z., Nittler, L. R., Starr, R. D., Crapster-Pregont, E. J., Peplowski, P. N., Denevi, B. W., Head, J. W., Byrne, P. K., Hauck, S. A., Ebel, D. S. and Solomon, S. C. (2015). Evidence for geochemical terranes on Mercury: Global mapping of major elements with MESSENGER's X-Ray Spectrometer. *Earth Planet. Sci. Lett.*, **416**, 109–120, doi:10.1016/j.epsl.2015.01.023.

Wurz, P. and Lammer, H. (2003). Monte-Carlo simulation of Mercury's exosphere. *Icarus*, **164**, 1–13.

Wurz, P., Whitby, J. A., Rohner, U., Martin-Fernandez, J. A., Lammer, H. and Kolb, C. (2010). Self-consistent modelling of

Mercury's exosphere by sputtering, micro-meteorite impact and photon-stimulated desorption. *Planet. Space Sci.*, **58**, 1599–1616, doi:10.1016/j.pss.2010.08.003.

Yakshinskiy, B. V. and Madey, T. E. (1999). Photon-stimulated desorption as a substantial source of sodium in the lunar atmosphere. *Nature*, **400**, 642–644.

Yakshinskiy, B. V. and Madey, T. E. (2000). Desorption induced by electronic transitions of Na from SiO_2: Relevance to tenuous planetary atmospheres. *Surf. Sci.*, **451**, 160–165.

Yakshinskiy, B. V. and Madey, T. E. (2004). Photon-stimulated desorption of Na from a lunar sample: Temperature-dependent effects. *Icarus*, **168**, 53–59.

Yakshinskiy, B. V. and Madey, T. E. (2005). Temperature-dependent DIET of alkalis from SiO_2 films: Comparison with a lunar sample. *Surf. Sci.*, **593**, 202–209.

Yakshinskiy, B. V., Madey, T. E. and Ageev, V. N. (2000). Thermal desorption of sodium atoms from thin SiO_2 films. *Surface Rev. Lett.*, **7**, 75–87.